A Modular Bacteriophage T4 Nanoparticle Platform Enables Rapid Design of Completely Protective Multivalent Mucosal Dual Vaccine Against COVID-19 and Flu

Jingen Zhu[1*], Jian Sha[2,3,4], Himanshu Batra[1], Swati Jain[1], Xiaorong Wu[1], Emily K. Hendrix[2], Paul B. Kilgore[2], Keer Sun[2], Kenneth S. Plante[2,3,4,5], Jessica A. Plante[2,3,4,5], Jordyn Walker[2,5], Pan Tao[8], Ashok K. Chopra[2,3,4,6,7*], and Venigalla B. Rao[1*]

[1]Bacteriophage Medical Research Center, Department of Biology, The Catholic University of America, Washington, DC, 20064, USA.

[2]Department of Microbiology and Immunology, [3]Galveston National Laboratory, [4]Institute for Human Infections and Immunity, [5]World Reference Center for Emerging Viruses and Arboviruses, [6]Center for Biodefense and Emerging Infectious Diseases, [7]Sealy Institute for Vaccine Sciences, University of Texas Medical Branch, Galveston, TX, 77555, USA.

[8]State Key Laboratory of Agricultural Microbiology, College of Veterinary Medicine, Huazhong Agricultural University, Wuhan, Hubei, China

*Correspondence: zhuj@cua.edu; achopra@utmb.edu; rao@cua.edu

One Sentence Summary:

A dual T4 phage nanoparticle vaccine induces potent mucosal immunity against SARS-CoV-2 and influenza viruses in mice via intranasal delivery and provides complete protection.

Abstract

The ongoing COVID-19 pandemic and recurrent influenza epidemics underscore the need for improved vaccine strategies, as the current vaccines face several challenges including limited mucosal protection, reduced efficacy against new variants, and waning immunity. We present an innovative bacteriophage T4 nanoparticle-based vaccine design that simultaneously targets both SARS-CoV-2 and influenza. It integrates three promising approaches: intranasal delivery for mucosal immunity, incorporation of multiple conserved antigens for broader protection, and nanoparticle presentation for enhanced B cell responses. By leveraging *in vivo* CRISPR genome engineering and *in vitro* SpyCatcher-SpyTag conjugation, this 120 x 86 nm T4-CoV-Flu vaccine nanoparticle incorporates 100s of antigen molecules from both pathogens, including SARS-CoV-2 spike ectodomain trimers, influenza hemagglutinin stem domain trimers, and M2e peptides on the capsid surface, while encapsulating matrix or nucleocapsid proteins inside. Intranasal administration of two doses of adjuvant-free T4-CoV-Flu vaccine to mice induced robust immune responses including high-titer IgG, secretory IgA, and neutralizing antibodies, balanced Th1/Th2 responses, and strong effector and memory T cell responses in both systemic and mucosal compartments. Notably, the vaccine elicited lung-resident $CD8^+$ T cells, diverse memory B cell populations, and conferred complete protection against lethal challenges with both SARS-CoV-2 and influenza viruses. Furthermore, the T4 platform's rapid adaptability allowed vaccine candidate generation in 2-3 weeks. Coupled with its scalability in bacterial systems, thermostability, and adjuvant- and needle-free delivery, T4 thus presents an extraordinary platform to design potent mucosal vaccines against pandemic threats, and to bring vaccine access to resource-limited settings across the globe.

INTRODUCTION

The COVID-19 pandemic, caused by severe acute respiratory syndrome coronavirus 2 (SARS-CoV-2), had a devastating impact on global health and economy, claiming over 7 million lives since 2019 (World Health Organization [WHO], https://covid19.who.int). Simultaneously, seasonal influenza (Flu) epidemics, caused by influenza A and B viruses, continue to pose a significant threat to public health, resulting in 290,000 to 650,000 deaths annually (*1*). Recent outbreaks of highly pathogenic avian influenza further raise concerns about the potential emergence of a novel pandemic strain (Centers for Disease Control and Prevention [CDC], https://cdc.gov/bird-flu/). The co-circulation of SARS-CoV-2 and influenza viruses is also concerning, as both pathogens share similar transmission routes, target tissues, and seasonal patterns, and can lead to more severe disease outcomes in co-infected individuals (*2-5*). Given these challenges, the development of vaccines capable of providing broad protection against both SARS-CoV-2 and influenza viral infections is of paramount importance.

The rapid deployment of injectable COVID-19 vaccines, such as the ones based on mRNA and adenoviral vectors achieving >90% efficacy in preventing severe disease, has been a remarkable achievement (*6, 7*). However, the emergence of SARS-CoV-2 variants with increased transmissibility and immune evasion characteristics, coupled with waning vaccine-induced immunity, has led to reduced vaccine effectiveness over time (*8-10*). Moreover, the current COVID-19 vaccines may have limitations in preventing viral transmission because of little to no mucosal immunity in the respiratory tract (*11-13*). Similarly, seasonal Flu vaccines face challenges related to antigenic drift and shift, requiring annual updates and revaccination to maintain protection against circulating strains (*14, 15*). The limited efficacy of current Flu vaccines against mismatched strains further highlights the critical need for newer and broadly protective vaccine designs (*16*).

At least three promising strategies emerged to address these challenges. First, development of intranasal mucosal vaccines has the potential to induce both systemic and

mucosal immunity, providing a first line of defense at the portal of entry, as well as to blunt transmissibility (*17, 18*). Preclinical studies with SARS-CoV-2 and influenza viruses have shown that intranasal vaccination can significantly reduce viral shedding and transmission compared to intramuscular vaccines (*18-22*). Despite this promise, development of intranasal vaccines remains a challenge (*23, 24*) and FluMist, a live attenuated influenza vaccine, is currently the only FDA-approved intranasal vaccine (*25*). Second, incorporation of multiple antigen targets into a vaccine formulation could mitigate the emergence of variants as well as provide broader protection (*20, 26, 27*). This would necessitate flexible and engineerable nanoparticle platforms, such as the virus-like nanoparticles (VLPs) (*28*). Third, multi-antigen presentation on a nanoparticle leads to increased avidity, B cell receptor cross-linking, as well as recruitment of low-affinity B cells, resulting in greater B cell clonotype diversity and breadth of neutralization (*29-33*). Here, we present a vaccine design that combines all these desirable features into one vaccine delivery platform using bacteriophage (phage) T4.

Of many synthetic or virus nanoparticles that are under investigation, phage T4 has emerged as one of the most versatile multivalent vaccine design platforms for several reasons (*34*). First, the 120 x 86 nm capsid of T4 phage provides one of the largest nanoparticle surfaces available to display multiple antigens (*35, 36*). Second, in addition to the two essential structural proteins, the major capsid protein gp23 (930 copies) and the vertex protein gp24 (55 copies), the T4 capsid is decorated with two non-essential outer capsid proteins Hoc (155 copies) and Soc (870 copies), both of which can be adapted to tether foreign antigens (*37-39*). Third, both Hoc and Soc have exquisite specificity and nanomolar affinity to bind to the capsid, allowing repetitive and symmetric display of large and full-length antigens on the capsid at high density. Furthermore, such VLPs mimic human viral pathogen-associated molecular patterns (PAMPs), to which the host immune system mounts a strong response (*36*). Fourth, in addition to surface display, up to ~1000 copies of antigens can be packaged inside the capsid by replacing the nonessential "internal proteins" (IPs) (*40-42*). Fifth, the T4 genome can be efficiently modified by CRISPR

editing (*43, 44*), for precise integration of antigen genes at specific loci for their *in vivo* expression and display during phage infection. Sixth, the temperature-stable T4 nanoparticle structure and its inexpensive manufacture and scalability could facilitate vaccine distribution without a cold-chain requirement (*45*), particularly to low- and middle-income communities across the world. Finally, our more than four decades of research led to effective vaccine designs against diverse bacterial and viral pathogens, including *Bacillus anthracis* (anthrax) (*46, 47*), *Yersinia pestis* (plague) (*48*), SARS-CoV-2 (COVID-19) (*45, 49*), and influenza (Flu) (*50*), thus, accumulating a substantial knowledge base to rapidly generate any vaccine of interest.

In this study, we present new advancements in phage T4 vaccine design, pushing the boundaries of this platform technology, to create a novel dual-pathogen mucosal vaccine against deadly respiratory viruses; SARS-CoV-2 and influenza. We incorporated five distinct antigens from two viruses into a single nanoparticle structure by combining *in vivo* CRISPR-engineered display/encapsulation with *in vitro* SpyCatcher-SpyTag conjugation (*51*). Furthermore, we incorporated relatively well-conserved antigens/domains with potential to generate broad immunity against diverse variants. These include: spike ectodomain (S-ecto) and nucleocapsid protein (NP) of SARS-CoV-2, hemagglutinin stem domain (HA-stem), the extracellular domain of the matrix protein 2 (M2e), and matrix protein 1 (M1) of influenza. S-ecto has many conserved epitopes, even though certain regions of the receptor binding domain (RBD) are under high selection pressure for mutation (*52, 53*), while NP is well-conserved and induces T cell responses that might provide cross-protection against different variants (*54-56*). Similarly, we chose the influenza HA-stem that is conserved in different subtypes (*57, 58*), as well as the conserved M2e and M1 antigens to further broaden cross-protection (*15, 59*). The multivalency of the T4-COVID-Flu (T4-CoV-Flu) vaccine, with a repertoire of foreign antigen molecules introduced into different locations of the phage structure, to our knowledge, has not been achieved with any other nanoparticle system.

This modular, multi-pronged, approach to vaccine design allowed rapid development of a needle-free, adjuvant-free, intranasal mucosal vaccine that induced robust mucosal as well as systemic humoral and cellular immune responses against both SARS-CoV-2 and influenza infections. These include high-titer IgG, secretory IgA, and neutralizing antibodies, balanced Th1 and Th2 responses, strong effector and memory T cell responses in both systemic and mucosal compartments, lung-resident CD8+ T cells, and diverse memory B cell populations, as well as complete protection against lethal challenges with prototypic viruses. The T4 platform's rapid adaptability to add variant antigens, scalability, and cost-effective production in bacterial hosts position it as a powerful protein-based vaccine design model to meet the demands of a countermeasure against future pandemic threats.

RESULTS

Overall design of T4-CoV-Flu dual vaccine candidates

Our overall design of T4-CoV-Flu dual vaccine candidates focused on the conserved and structural elements of both SARS-CoV-2 and influenza viruses. Taking advantage of the above-mentioned features of the phage T4 platform, we set out to strategically incorporate several antigen targets into the T4 nanoparticle structure (Fig. 1; fig. S1, A and B). These include: (1) the mammalian cell-expressed and prefusion-stabilized S-ecto trimers and HA-stem trimers, which would be displayed on the capsid exterior using the SpyCatcher-Spytag conjugation *in vitro* (*51*), (2) the 24-amino acid (aa) influenza M2e peptide fused to the tips of the 180 Å-long hoc fibers, which would be displayed through *in vivo* assembly, and (3) the conserved SARS-CoV-2 NP or influenza M1 proteins, which would be packaged *in vivo* in the interior of the capsid.

In vitro assembly was used for displaying the envelope trimers because doing so *in vivo* during phage infection in *E. coli* was proven to be challenging for several reasons, such as poor expression and folding, and lack of post-translational modifications. Therefore, the mammalian

cell-expressed proteins were biochemically characterized and displayed on the capsid through *in vitro* assembly, which also ensured the structural and functional integrity of the antigen epitopes (Fig. 1B and 1C; fig. S1C).

On the other hand, the M2e, NP, and M1 antigens requiring no essential post-translational modifications were well-expressed during phage infection when the target genes were inserted into the T4 genome by CRISPR genome engineering under the control of strong phage promoters. The expressed proteins were then either displayed on the capsid due to their fusion to Hoc or Soc, or packaged inside the capsid due to their fusion to the capsid targeting sequence (CTS) (Fig. 1A and 1B).

To maximize expression, we employed codon optimization because significant differences in nucleotide content exist between the T4 phage genome (65% AT + 35% GC) and the *E. coli* host genome (49% AT + 51% GC) (Fig. 2A). Comparison of display efficiencies showed that the T4 codon-optimized Soc-SpyCatcher exhibited significantly higher display amounts (Fig. 2, B and C) and correspondingly higher conjugation efficiency of SpyTagged trimers (Fig. 2, D and E).

We performed extensive series of experiments to optimize the T4 platform for efficient *in vivo* display on the capsid surface and/or encapsulation in the capsid interior using diverse antigens from SARS-CoV-2 and influenza, as well as several other model antigens, nanobodies, and fluorescent proteins (Fig. 2, F to H). Notably, we achieved display of up to 180 copies of functional nanobodies per capsid, demonstrating the platform's potential for applications beyond traditional vaccines. These optimizations were crucial for enabling the efficient production of our multivalent T4-CoV-Flu dual vaccine and highlight the broader potential of the T4 platform for rapid vaccine development against various pathogens.

Finally, a series of vaccine candidates containing combinations of SARS-CoV-2 and Flu antigens were rapidly produced and tested in a mouse model that allowed the selection of a candidate that showed the highest efficacy as a dual CoV-Flu vaccine.

Production of T4-CoV-Flu vaccine candidates

The T4-CoV-Flu vaccine candidates were produced by a two-step process; first engineer recombinant phages containing displayed or encapsidated antigens by *in vivo* expression, then perform *in vitro* assembly and conjugation using purified mammalian cell-expressed antigens (Fig. 1). For the former, gene segments encoding influenza M1 (or NP), M2e, and SpyCatcher were inserted into specific loci of the T4 genome; CTS-IP, Hoc, and Soc, respectively, using CRISPR-targeted genome editing (fig. S1, A and B). SDS-PAGE and Western blot analyses of CsCl-gradient purified recombinant phage particles showed successful incorporation and assembly of each of these antigen components (Fig. 3A). Molecular weight determinations further confirmed M2e-Hoc fusion, Soc-SpyCatcher conjugation to SpyTagged S-ecto and HA-stem trimers, and packaging of M1 and NP proteins.

Approximately 40 copies of M1 or 100 copies of NP, 90 copies of M2e, and 205 copies of Soc-SpyCatcher were co-incorporated into a single T4 nanoparticle (Fig. 3A). It is noteworthy that such a multi-antigen *in vivo* engineering of phage has not been reported so far, pointing to the versatility of the T4 vaccine design platform. Notably, incorporation of these antigens did not affect phage yield, which was in the order of 10^{14}-10^{15} phage particles per liter of *E. coli* culture. Assuming about 10^{11}-10^{12} particles per vaccine dose, this reflects up to ~10^3 to 10^4 doses per liter of *E. coli*, which might be further improved in an industrial-scale fermenter under optimal nutrient and aeration conditions.

In the second step, S-ecto and HA-stem envelope trimers containing C-terminal SpyTag fusions were expressed and purified from Chinese hamster ovary (CHO) cells and human embryonic kidney 293 F (HEK 293F) cells, respectively (fig. S1C), and conjugated *in vitro* to Soc-SpyCatcher arrayed on T4 capsid. Both S-ecto and HA stem trimers can be efficiently conjugated to the capsid, reaching saturation at a molar ratio of 1:1 of trimer to Soc binding sites, resulting in approximately 118 copies of S-ecto trimer or 107 copies of HA-stem trimer per capsid (fig. S2).

Since Soc-SpyCatcher subunits are located at the quasi-3-fold axes of the T4 icosahedral structure, the conjugated trimers would occupy symmetric positions on the nanoparticle surface.

To achieve optimal antigen density and ensure efficient co-display of both S-ecto and HA-stem trimers on the same nanoparticle, the ratios of SpyTagged HA-stem and S-ecto trimers to SpyCatcher sites were systematically titrated (Fig. 3, B and C). The data showed that the display efficiency and copy number could be tuned by adjusting the ratios of trimers to binding sites and/or the sequence of addition of the two types of trimers. Three different sequences were explored (Fig. 3, B and C): 1) HA-stem added first, incubated, and then S-ecto added; 2) S-ecto added first, incubated, and then HA-stem added; and 3) both HA-stem and S-ecto added simultaneously while varying the ratios.

The results showed approximately equivalent co-display of S-ecto and HA-stem trimers on a single capsid (~56 copies of S-ecto trimer and ~46 copies of HA-stem trimer) when S-ecto trimers were added first at a 0.25:1 ratio, incubated, and then HA-stem trimers were added at a 1:1 ratio. Not surprisingly, the major size difference between the S-ecto trimer (433.5 kDa) and the HA-stem trimer (100 kDa) affected the display efficiency. Displaying first the 4.3-times larger S-ecto trimers left a significant fraction of binding sites unoccupied probably due to steric hindrance, which were then filled by the much smaller HA-stem trimers (46 copies). The maximum copy number attained was ~100 trimers per capsid. In the opposite sequence, when HA-stem trimers were added first, fewer binding sites were left unoccupied for the much larger S-ecto trimers leading to ~35 copies per capsid (Fig. 3, B and C).

The above two-step process leverages the versatility of both the CRISPR-based *in vivo* engineering and SpyCatcher-Spytag-based *in vitro* conjugation, enabling the incorporation of multiple desired antigens into a single nanoparticle at high copy numbers (Fig. 3D). Furthermore, the ability to generate desired combination of antigens and tuning their copy numbers highlight the flexibility and modularity of the phage T4 vaccine platform.

Intranasal administration of T4-CoV-Flu vaccine candidates elicited robust systemic humoral immune responses

To evaluate the immunogenicity of the T4-CoV-Flu vaccine candidates, the recombinant phages were purified by two CsCl-gradient centrifugations and suspended in simple phosphate-buffer-saline (PBS, pH 7.4) with no adjuvant or stabilizing chemicals. Such preparations contained low levels of endotoxin (~10 endotoxin units per 10^{11} phage), well below the FDA-recommended levels (*60*). The ability of these phages to induce humoral antibody responses against various SARS-CoV-2 and influenza antigens was tested in the BALB/c mouse model by intranasal administration (Fig. 4A).

Groups of mice received two intranasal doses of 2.5 x 10^{11} phage particles of various vaccine candidates; T4-CoV-NP-S-ecto, T4-Flu-M2e, T4-Flu-M1-M2e-HA-stem, T4-CoV-NP-S-ecto/Flu-HA-stem, or T4-CoV-S-ecto/Flu-M1-M2e-HA-stem. Mice receiving T4 phage backbone lacking any CoV or Flu antigens were used as negative controls, while a mixture of soluble S-ecto and HA-stem trimers served as a positive control. In a previous study, intranasal vaccination of unadjuvanted CoV-2 S-ecto protein was reported to induce protective mucosal immunity (*61*).

All the T4-CoV-Flu candidates elicited high titers of serum antibodies against the externally displayed antigen components, including S-ecto, HA-stem, and M2e (Fig. 4, B to E; fig. S3, A and B). The T4 vector-specific antibodies for reasons unknown mildly cross-reacted with S-ecto trimer. Hence, RBD which exhibits no significant cross-reactivity with T4 antibodies was also included in our analyses. The endpoint IgG titers against RBD and HA-stem trimers were at the order of 10^5-10^6, ~10-fold higher than that induced by soluble trimers. Unlike the soluble trimers which bias the response to IgG1 antibodies, the T4-CoV-Flu vaccine candidates generated high and balanced levels of both IgG1 and IgG2a responses.

Interestingly, the HA-specific antibody titers in the high occupancy HA-stem display group (T4-M1-M2e-HA) were approximately 5-fold higher than the titers in the half-amount HA-stem display group (T4-M1-M2e-HA-S or T4-NP-HA-S) (Fig. 4D), indicating a dose-dependent

response. Notably, compared to soluble trimers and recombinant subunit vaccines in general that show a strong bias towards inducing type 2 helper (Th2) antibody responses, the T4-CoV-Flu vaccine candidates induced high levels of both IgG2a and IgG1 responses (fig. S3, C and D). Such a balanced Th1/Th2 antibody profile is desirable for minimizing the risk of vaccine-enhanced respiratory disease (*62, 63*). The Th1/Th2 balanced response may be attributed to the intrinsic adjuvant properties of the T4 phage nanoparticle, which can stimulate innate immune responses and promote antigen presentation by antigen-presenting cells (*34, 36, 45, 49*).

In addition to the antibodies targeting the displayed antigens, IgG responses were also detected against the internally packaged NP and M1 proteins, but at much lower levels (fig. S4). This means that the encapsidated antigens unlike the well-exposed surface epitopes were not well presented to the immune system for eliciting humoral responses.

Remarkably, the surface exposed S-ecto and HA-stem antigens induced potent serum IgA responses with endpoint titers ranging from 10^4 - 10^5, ~50-100 fold higher than that induced by the soluble trimers (Fig. 4, B to E). High titers of IgA antibodies are considered desirable for the clinical efficacy of vaccines because they are reported to possess anti-inflammatory activity, and are more effective than IgG in neutralizing the SARS-CoV-2 virus in the early stages of infection (*64*). Moreover, IgA is the predominant antibody isotype at mucosal surfaces and plays a crucial role in protecting against transmission of respiratory pathogens (*65*).

To independently evaluate the observed high immunogenicity of T4-CoV-Flu vaccine candidates, we immunized transgenic mice expressing the human angiotensin-converting enzyme 2 receptor (hACE2), the primary entry receptor for SARS-CoV-2. Consistent with the results described above in BALB/c mice, the T4-CoV-Flu vaccine candidates elicited similarly potent antibody responses against S-ecto and HA antigens in hACE2-transgenic AC70 mice (fig. S5), indicating the effectiveness of this vaccine strategy in an animal model that more closely mimics human infection. Importantly, these antibodies also showed strong virus-neutralizing activity as determined by the Vero E6 cell Focus Reduction Neutralization Test (FRNT) assay

using the live SARS-CoV-2 US-WA-1/2020 strain (Fig. 4F), underscoring the potential of these T4-based vaccines to confer protective immunity.

Collectively, the above datasets showed robust and simultaneous induction of antibodies against two distinct respiratory viral pathogens, highlighting the potential of intranasal T4 immunization for multivalent vaccine development.

T4-CoV-Flu vaccines induced strong mucosal humoral immune responses

To assess if the T4-CoV-Flu vaccines elicited mucosal antibody responses, we collected bronchoalveolar lavage fluid (BALF) and determined the antigen-specific antibody titers by ELISA (Fig. 4). Remarkably, all the T4-CoV-Flu phages elicited high titers of IgG, both IgG1 and IgG2a subclasses, and secretory IgA (sIgA) in BALF against the displayed antigens, including RBD/S-ecto, HA-stem, and M2e (Fig. 5). The mucosal IgG included balanced Th1-biased IgG2a and Th2-biased IgG1 subtype antibodies (Fig. 5), consistent with the balanced Th1/Th2 profile observed in the systemic antibody responses (Fig. 4). Moreover, the mucosal antibody titers induced by the T4-CoV-Flu phage nanoparticles were 5- to 25-fold higher than those induced by soluble trimers. This again highlights the effectiveness of T4-vectored mucosal delivery in stimulating local antibody responses without the need for additional adjuvants. The induction of high-titer mucosal IgG and sIgA antibodies is crucial for neutralizing the invading respiratory viruses at the portal of entry, reducing the risk of infection, disease severity, and transmission (*64, 66*).

Polyfunctional T and B cells as well as memory responses in the lung and spleen stimulated by T4-CoV-Flu vaccines

In addition to humoral immunity, T-cell-mediated responses play a critical role in providing long-term protection against respiratory viruses (*67, 68*). To evaluate these responses elicited by the T4-CoV-Flu vaccines, we determined the phenotype and functionality of antigen-specific T cells in the spleen and lungs of i.n. immunized mice. Compared to T4 control group, intracellular

cytokine staining revealed that T4-CoV-Flu (T4-M1-M2e-HA-S-ecto) i.n. vaccination led to a significant increase in the frequencies of S-ecto- and HA-stem-specific $CD4^+$ and $CD8^+$ T cells that produce IFNγ, IL-2, TNFα, and IL-17A in both spleen (Fig. 6, A to D) and lungs (Fig. 6, E to H). In contrast, the frequencies of antigen-specific T cells producing IL-4 and IL-5 did not significantly increase in all vaccinated groups except in mice immunized with T4-M1-M2e-HA-S that had higher splenic HA-specific $CD4^+$ cells producing IL-4 and IL-5 (Fig. 6C). Most importantly, mice immunized with T4-CoV-Flu had overall higher cytokine positive T cells specifically for IL-2, TNFα and IL-17 in comparison with soluble trimer vaccinated mice (Fig. 6, A to H). These results indicated the T4-CoV-Flu-mediated induction of Th1 and cytotoxic T cell responses, which are desirable for COVID-19 vaccines, contributed to viral clearance and reduced disease severity (*69, 70*).

Furthermore, T4-CoV-Flu vaccination led to a significant increase in the proportions of antigen-specific effector memory (T_{EM}) $CD8^+$ and $CD4^+$ T cells in the spleen (Fig. 6, I to L), as well as tissue-resident memory (T_{RM}) $CD8^+$ T cells in the lungs (Fig. 6, M and N). These memory T cell subsets are critical for providing rapid and effective recall responses upon re-exposure to the pathogen and are essential for maintaining long-term protective immunity (*71*). However, S-ecto- and HA-stem-specific lung-resident $CD4^+$ T_{RM} cells were not significantly increased in the T4-CoV-Flu vaccinated groups when compared to the T4 control (fig. S6, A and B), suggesting that the T4-CoV-Flu vaccine may be more effective at inducing $CD8^+$ T_{RM} cells than $CD4^+$ T_{RM} cells in the lungs. The significant induction of lung-resident $CD8^+$ T_{RM} cells by the T4-CoV-Flu vaccine is particularly promising, as these cells can provide immediate protection against respiratory viruses at the site of infection, even in the absence of circulating antibodies (*72*).

The induction of memory B cells is crucial for maintaining long-term antibody production and providing rapid and enhanced antibody responses upon re-exposure to the pathogen (*73*). The T4-CoV-Flu vaccine induced a significant increase in diverse memory B cells when compared to the soluble trimer vaccine (Fig. 6O; fig. S6C). Notably, the vaccine elicited diverse memory B

cell populations, including $CD73^+$, $CD80^+$, $PDL2^+$, and $CD73^+CD80^+PDL2^+$ cells, all at higher levels than in control groups (Fig. 6O; fig. S6C). This combination of markers allows for the study of different functional aspects of memory B cells, such as immune regulation (CD73, PDL2) and activation (CD80). The diverse memory B cell response is consistent with reported studies showing that multi-antigen presentation on nanoparticles leads to greater B cell clonotype diversity and breadth of neutralization (*29, 30*). The enhanced diversity and quantity of memory B cells indicate the T4-CoV-Flu vaccine's ability to elicit robust and potentially more broadly protective long-lasting adaptive immune responses.

Taken together, the above results demonstrated that i.n. vaccination with T4-CoV-Flu phages not only induced potent antibody responses, but also stimulated polyfunctional T cell responses in both systemic and mucosal compartments. Induction of antigen-specific $CD4^+$ and $CD8^+$ T cells producing Th1 and Th17 cytokines, diverse memory B cells, as well as generation of effector and lung tissue-resident memory $CD8^+$ T cells, provided a compelling rationale for developing T4-CoV-Flu vaccine as a mucosal vaccine against multiple respiratory viruses.

T4-CoV-Flu intranasal vaccine provided complete protection against lethal SARS-CoV-2 and influenza infections

To evaluate the protective efficacy of the T4-CoV-Flu vaccine, we challenged the immunized mice with lethal doses of either ancestral SARS-CoV-2 or influenza A/Puerto Rico/8/1934 (H1N1 PR8) virus and monitored their body weight and survival over time (Fig. 7A). In the SARS-CoV-2 challenge experiment, hACE2 mice vaccinated with T4 phage control rapidly lost weight and succumbed to the infection in 6 days. In contrast, mice immunized with T4-CoV (T4-NP-S) or T4-CoV-Flu (T4-M1-M2e-HA-S or T4-NP-HA-S) were completely protected against both weight loss and mortality (Fig. 7, B and C). Notably, the T4-CoV and T4-CoV-Flu vaccines provided superior protection compared to vaccination with soluble S-ecto/HA-stem trimers, which

only conferred partial protection (60% survival rate) (Fig. 7, B and C), further highlighting the effectiveness of the T4-vectored mucosal delivery.

Similarly, in the influenza H1N1 challenge experiment, T4 control mice rapidly lost weight and succumbed to the infection in about 8 days. However, mice vaccinated with multivalent T4-Flu (T4-M1-M2e-HA) or T4-CoV-Flu (T4-M1-M2e-HA-S or T4-NP-HA-S) were completely protected against both weight loss and mortality. In contrast, soluble S-ecto/HA-stem trimers provided only low and partial protection, with a mere 20% survival rate (Fig. 7, D and E). Although the HA-specific serum antibody titers in the T4-M1-M2e-HA group were higher than the titers in the T4-M1-M2e-HA-S group (Fig. 4), there was no difference in body weight change between the two groups over 21 days following challenge (fig. S7A).

The co-display of HA-stem with other influenza antigens, such as M1 and M2e, in the T4-CoV-Flu vaccine (T4-M1-M2e-HA-S) contributed to improved protection, as evident by faster body weight recovery after challenge compared to the monovalent HA-stem antigen in the T4-NP-HA-S vaccine (fig. S7, B and C). Remarkably, T4 displaying M2e alone was able to confer complete protection against the H1N1 challenge, and incorporation of additional influenza antigens, M1 and HA stem, further significantly improved body weight recovery (fig. S7D). These findings supported the value of T4-arrayed multivalent display in enhancing the potency of vaccine-induced protection.

The above challenge studies demonstrated that nasal T4-CoV-Flu dual nanovaccines are effective in providing complete protection against lethal SARS-CoV-2 and influenza infections in mice. Thus, from the body of evidence described above, it can be concluded that the high-capacity antigen loading and plug-and-play nature of this platform, coupled with its ability to induce robust systemic and mucosal protective immunity, positions it as a promising needle-free vaccine delivery vehicle for combating respiratory pathogen pandemic and epidemic threats.

DISCUSSION

Our study represents a significant advancement in protein-based vaccine technology by leveraging the unique properties of phage T4 to create a multivalent, adjuvant-free, intranasal COVID-Flu dual vaccine. This approach addresses several key limitations of current vaccine strategies and offers a promising platform for rapid response to emerging respiratory threats.

The T4-CoV-Flu vaccine demonstrates remarkable versatility in antigen presentation, incorporating five distinct antigens from SARS-CoV-2 and influenza viruses into a single nanoparticle. We achieved the co-display of approximately 56 copies of S-ecto trimer and 46 copies of HA-stem trimer per capsid, along with 90 copies of M2e and encapsulation of 40 copies of M1 or 100 copies of NP. This level of multivalency, combining conserved epitopes from both viruses, represents a significant step towards developing broadly protective vaccines capable of addressing viral antigenic drift and the emergence of new variants. The ability to rapidly engineer and produce such complex vaccine candidates, with phage yields of up to 10^{14} -10^{15} particles per liter of *E. coli* culture, highlights the potential of the T4 platform for swift adaptation to evolving pandemic threats.

One of the most striking features of our vaccine is its ability to induce robust mucosal immunity, a critical factor in preventing respiratory virus transmission that is often lacking in current injectable vaccines (*19, 20, 22*). We observed elevated levels of sIgA in the BALF of vaccinated mice, far surpassing those induced by soluble trimers. This localized immune response, combined with strong systemic antibody production, provides a dual layer of protection that could significantly reduce both infection and transmission rates.

The balanced Th1/Th2 immune response elicited by the T4-CoV-Flu vaccine is another key advantage over other vaccines. We observed high levels of IgG2a and IgG1 antibodies, with balanced ratios for both S-ecto and HA-specific responses. This balanced response is crucial for effective viral clearance and may reduce the risk of vaccine-enhanced respiratory diseases (*63*).

Furthermore, we demonstrated the induction of polyfunctional T cell responses, including a significant increase in the frequencies of antigen-specific $CD4^+$ and $CD8^+$ T cells producing IFNγ, IL-2, TNFα, and IL-17A in both spleen and lungs. Notably, we observed a marked increase in tissue-resident memory $CD8^+$ T cells in the lungs of T4-CoV-Flu vaccinated mice suggesting potential for long-lasting local immunity (*72*). Additionally, the vaccine induced diverse memory B cell populations with CD73, CD80, and PDL2 expression, suggesting enhanced immune regulation and activation potential that may contribute to broader, more durable protection against viral variants.

The complete protection observed in mice against lethal challenges of both SARS-CoV-2 and influenza viruses is a powerful demonstration of the vaccine's efficacy. All mice vaccinated with T4-CoV or T4-CoV-Flu constructs survived the SARS-CoV-2 challenge without weight loss, compared to only partial survival in the soluble trimer group. Similarly, all vaccinated mice survived the influenza challenge versus a low survival rate in the soluble trimer group. This dual protection, achieved without the need for adjuvants, suggests that the intrinsic properties of the T4 nanoparticle may serve as a natural immune stimulant.

From a translational perspective, the T4-CoV-Flu vaccine offers several advantages that could significantly impact clinical practice and public health strategies. The intranasal administration route not only induces robust mucosal immunity but also offers the potential for needle-free vaccination, which could improve vaccine acceptance and simplify mass vaccination campaigns (*74*). The stability of the T4 nanoparticle at room temperature (*45*) could greatly facilitate vaccine distribution, particularly in resource-limited settings, by reducing cold chain requirements.

The modular nature of the T4 platform, allowing for the rapid incorporation of new antigens, positions this technology as a valuable tool for pandemic preparedness. We demonstrated that new recombinant phages could be generated in 2-3 weeks using our CRISPR-based engineering approach, which could dramatically reduce response times during future outbreaks. Moreover,

the potential to combine antigens from multiple pathogens in a single vaccine could streamline immunization programs, improving coverage and reducing the logistical burden of multiple vaccinations.

However, several important questions and challenges remain to be addressed as we move towards clinical translation. While our results in mice are highly encouraging, studies in larger animals, particularly non-human primates, will be crucial to validate the vaccine's safety and efficacy in a model more closely resembling human physiology.

The mechanism by which the T4 nanoparticle enhances immune responses without traditional adjuvants warrants further investigation. The multivalent and symmetrized display of antigens on the T4 capsid may enhance B cell receptor cross-linking and recruitment of low-affinity B cells, leading to greater B cell clonotype diversity and breadth of neutralization (*30, 32, 33*). Understanding these intrinsic immunostimulatory properties could provide valuable insights for the design of future mucosal nano-vaccine platforms.

Looking ahead, the evaluation of cross-protection against a broader range of SARS-CoV-2 variants and influenza strains will be critical to assess the breadth of protection. Studies on the duration of immunity, particularly the longevity of mucosal and tissue-resident memory responses, will inform vaccination strategies.

The global health implications of this technology are substantial. A single nasal vaccine protecting against both COVID-19 and influenza could significantly reduce the burden on healthcare systems, particularly during winter months when both viruses circulate. The potential for room-temperature stable, needle-free vaccines could revolutionize vaccination programs in low- and middle-income countries, contributing to greater global health equity.

In conclusion, our T4-CoV-Flu intranasal vaccine represents a promising new approach in the fight against respiratory pathogens. Unlike many live or live-attenuated intranasal viral vaccine models currently under development, which can face challenges related to preexisting immunity and safety concerns, the noninfectious T4 platform presents a promising alternative approach. By

stockpiling a recombinant T4 phage scaffold containing *in vivo*-expressed and displayed antigens, any pandemic antigen(s) can be rapidly produced in bacterial, insect cell, or mammalian cell expression systems and loaded on the capsid by simple mixing of the two to create a variety of multivalent vaccines. Such protein-based T4 mucosal vaccines can be inexpensively and rapidly manufactured in response to emerging pandemic threats. Importantly, they can be mass-distributed without cold-chain requirements to resource-limited settings and to military personnel, even in remote areas of the world.

MATERIALS AND METHODS

DNA, bacteria, bacteriophages, and viruses

The pET28b vector (Novagen, MA) was utilized to construct donor plasmids. Previously established methods (*43, 44, 75*) were followed for constructing the LbCas12a and SpCas9 spacer plasmids. GeneArt (Thermo Fisher, MA) synthesized the donor DNA fragments that were pre-optimized with T4 codons for phage display. Plasmids containing the WT SARS-CoV-2 S-ecto-6P gene were generously provided by J. S. McLellan from the University of Texas, Austin. Plasmids with SpyCatcher/SpyTag sequences were obtained from Addgene (MA) (#133449).

For all cloning procedures, *E. coli* DH5α [hsdR17 (rK–mK$^+$) sup2] (New England Biolabs, MA) was employed. The *E. coli* B40 (sup1) strain was used to propagate and produce wild-type and various recombinant phages.

The SARS-CoV-2 US-WA-1/2020 strain was obtained through CDC and is available at the World Reference Center for Emerging Viruses and Arboviruses, Galveston National Laboratory, UTMB. Influenza A virus (H1N1) strain A/PR/8/34 was propagated in specific pathogen-free chicken embryonated eggs and was purchased from the AVSBio (Norwich, CT). This strain was originally isolated in 1934 from a human patient in Puerto Rico.

CRISPR engineering of T4 phage genome

The bacteriophage T4 genome was modified using a CRISPR-Cas-assisted editing approach as described previously with some modifications(*43, 44, 49*). Briefly, guide RNAs for either the Cas9 nuclease from *Streptococcus pyogenes* or the Cas12a (Cpf1) nuclease from *Lachnospiraceae* bacterium were designed to target non-essential regions of the T4 genome selected for insertion of the SARS-CoV-2 and influenza viral genes. These regions included the Hoc, Soc, IPII, and IPIII loci (Fig. 1). The protospacer sequences were cloned into the respective CRISPR plasmids containing pCas9 or pCas12a nuclease gene, necessary trans-activating CRISPR RNA (tracrRNA), or direct repeat sequences. In parallel, donor plasmids were synthesized comprising the codon-optimized exogeneous genes flanked by ~500 bp T4 homology arms matching the genomic insertion sites. The CRISPR and donor plasmids were co-transformed into chemically competent *E. coli* strains (DH5α or B40) and used to generate recombinant phages harboring the desired gene insertions following infection with wild-type T4 phage. Escaped phages that avoided cleavage by Cas9 or Cas12a due to successful incorporation of the donor sequence were enriched through a second round of infection in the CRISPR-expressing cells. Multiple iterative rounds of CRISPR-mediated editing and phage infection were performed to combine several modifications into a single phage genome, yielding the final multivalent T4-CoV, T4-Flu, or T4-CoV-Flu vaccine constructs. Genomic insertions were verified by PCR and Sanger sequencing. High-titer purified phage stocks were prepared by CsCl gradient ultracentrifugation.

Phage production and purification

T4-CoV, T4-Flu, and T4-CoV-Flu phages were produced and purified as previously described (*45, 49*). Briefly, phages were propagated in *E. coli* strain B40 cultured in Moore's medium. After infection and lysis, phages were harvested by centrifugation and purified using two rounds of CsCl gradient ultracentrifugation, followed by dialysis and 0.22-μm filtration. Phage concentration and antigen display were quantified by 4-20% SDS-PAGE.

Expression and purification of prefusion-stabilized spike and HA stem trimers

Prefusion-stabilized ectodomain trimers of the SARS-CoV-2 spike protein (aa 1-1208 of the Wuhan-Hu-1 strain) with six proline substitutions was purified as described (*45*). The influenza HA stem construct was designed based on the A/Puerto Rico/8/1934 (H1N1) virus. The HA stem sequence was genetically fused to a N-terminal 8x histidine tag and a C-terminal SpyTag003 peptide to enable covalent conjugation to SpyCatcher-displaying phages. The SpyTagged HA stem sequence was cloned into the pAAV vector and expressed by transient transfection into HEK293F cells using 293fectin reagent (Thermo Fisher). Trimeric HA-stem trimers were purified from the clarified culture supernatants by immobilized metal affinity chromatography (IMAC) using HisTrap FF columns (Cytiva, MA) followed by size exclusion chromatography (SEC) on a HiLoad 16/600 Superdex 200 (preparation grade) column (GE Healthcare, IL). The purified trimers were flash-frozen in liquid nitrogen and stored at -80°C.

***In vitro* conjugation of spike and stem trimers to T4 phage scaffold**

The display of Spytag-containing spike and HA stem trimers on the T4-SpyCatcher phage *in vitro* was assessed using a modified co-sedimentation technique (*49, 76*). In brief, phage particles were purified by two rounds of CsCl gradient centrifugation, filtered through a 0.22-µm filter, and sedimented at 34,000g for 30 minutes in Protein-LoBind Eppendorf tubes. The sedimented phages were then washed twice with sterile PBS buffer (pH 7.4) and resuspended in the same buffer. To remove any aggregates, S-ecto or HA-stem trimers were also sedimented at 34,000g for 15 minutes. Subsequently, T4-SpyCatcher phages were incubated with S-ecto and/or HA-stem trimers, either sequentially or simultaneously, at 4°C for 1-2 hours. The mixtures were centrifuged at 34,000g for 30 minutes to remove unbound proteins in the supernatants. The phage pellets were washed twice with excess PBS to eliminate any unbound protein and minor contaminants. The pellets containing the displayed proteins were then incubated at 4°C overnight and resuspended in PBS. The resuspended pellets were analyzed using a Novex 4-20% gradient SDS-PAGE mini gel (Thermo Fisher) to quantify the S-ecto or HA-stem trimer copies. After

staining with Coomassie Blue R-250 (Bio-Rad, CA) and destaining, the protein bands on the SDS-PAGE gels were scanned and quantified using a ChemiDoc MP imaging system (Bio-Rad) and Image J software. The copy numbers of SpyCatcher and displayed spike or HA stem trimer molecules per capsid were calculated using gp18 (major tail sheath protein; 138 copies) or gp23 (major capsid protein; 930 copies) as internal controls, along with S-ecto or HA-stem trimer protein standards.

Western Blot (WB) analysis

Following three freeze-thaw cycles and Benzonase treatment, purified phage particles were boiled in the SDS loading buffer for 10 minutes. They were then separated using 4-20% SDS-PAGE and transferred onto a polyvinylidene difluoride (PVDF) membrane (Bio-Rad). The membrane was processed for binding of NP- or Hoc- specific antibodies as described previously (*49*). The enhanced chemiluminescence (ECL; Bio-Rad) bands were visualized using the Bio-Rad Gel Doc XR+ System and analyzed using Image Lab software.

Animal vaccination

Animal experiments adhered strictly to the guidelines set forth in the Guide for the Care and Use of Laboratory Animals by the National Institutes of Health. The protocols received approval from the Institutional Animal Care and Use Committee (IACUC) of both the Catholic University of America (Washington, DC; Office of Laboratory Animal Welfare assurance number A4431-01) and the University of Texas Medical Branch (UTMB, Galveston, TX; Office of Laboratory Animal Welfare assurance number A3314-01). SARS-CoV-2 virus infections were conducted within an animal biosafety level 3 (ABSL-3) containment facility while influenza virus infections were conducted within an animal biosafety level 2 (ABSL-2) containment facility, both at UTMB under approved protocols.

Female BALB/c mice (Jackson Laboratory, ME) or hACE2-transgenic AC70 mice (Taconic Biosciences, NY), aged 4-6 weeks, were randomly assigned to groups (5 animals per group) and allowed a 14-day acclimation period. For intranasal (i.n.) vaccinations, mice were anesthetized

via inhalation of isoflurane. They were then administered with 2.5 x 10^{11} T4-CoV, T4-Flu, or T4-CoV-Flu phage particles in 50 µL of PBS (25 µL per nare). Two vaccine doses were given 3 weeks apart following a prime-boost regimen. Negative control groups received T4 backbone vector phage without antigens. A mixture of equal amounts of soluble HA-stem and S-ecto trimers served as the positive control. Blood samples were collected from each animal and the sera were stored at -80°C.

SARS-CoV-2 and influenza H1N1 challenge

For animal challenge studies, mice were ear-tagged and weighed before the challenge to monitor individual weights throughout the study. Animals were anesthetized with isoflurane and then 50µL of viral challenge stock was administered (25 µL to each nare) followed by a 20µL PBS wash. For animals receiving SARS-CoV-2 US-WA-1/2020, the challenge dose was $100LD_{50}$ ($3.3x10^2$ $TCID_{50}$) (*45, 77*). For animals challenged with Influenza, the challenge dose was $8.8x10^3$ PFU (~$10LD_{50}$). Animals were weighed daily and scored for clinical signs of disease according to our approved IACUC protocols.

Collection of Bronchoalveolar Lavage Fluid (BALF)

Around 21 days post influenza A PR8 strain challenge, survivals were euthanized, and BALF was collected using a method adapted from a prior study (*78*). In brief, the tracheas were exposed by dissecting the salivary glands. A small cut was made on the trachea's ventral side, and a blunt 26G needle, secured by tying the trachea around the catheter with floss, was inserted into the trachea. The lungs were then flushed with 600 µL of PBS using a 1-mL syringe, and the BALF samples were collected.

Antibody ELISAs

To quantify SARS-CoV-2 spike, RBD, and NP-specific antibodies, as well as influenza HA and M2e-specific IgG, IgG1, IgG2a, and IgA antibodies in serum and BALF, we employed an enzyme-linked immunosorbent assay (ELISA). High-binding 96-well plates (Evergreen Scientific, CA) were coated overnight at 4°C with 100 µL of 1 µg/mL purified recombinant spike, RBD, NP,

HA stem, or M2e peptide diluted in coating buffer (0.05 M sodium carbonate-sodium bicarbonate, pH 9.6). The plates were washed twice with PBS buffer, then blocked with 200 µL per well of PBS (pH 7.4) containing 5% BSA at 37°C for 2-3 hours. Serum and BALF samples were subjected to a 5-fold serial dilution, starting with an initial 100-fold dilution in PBS containing 1% BSA. Subsequently, 100 µL of the diluted samples were added to each well, and the plates were incubated at 37°C for 1 hour. The plates were then washed five times with PBST (PBS with 0.05% Tween 20). Following this, a secondary antibody, diluted 1:10,000 in PBS with 1% BSA (100 µL/well), was added. This included goat anti-mouse IgG-HRP, goat anti-mouse IgG1-HRP, goat anti-mouse IgG2a-HRP, or goat anti-mouse IgA-HRP (Thermo Fisher). After another hour of incubation at 37°C and five additional washes with PBST, the plates were developed using the TMB (3,3',5,5'-tetramethylbenzidine) Microwell peroxidase substrate system (KPL, MA; 100 µL) for 5 to 10 minutes. The reaction was stopped by adding 100 µL of TMB BlueSTOP solution (KPL). The absorbance at 650 nm was read within 30 minutes using a VersaMax spectrophotometer. The endpoint titer was defined as the highest reciprocal dilution of serum or BALF that produced an absorbance greater than 2-fold the mean background of the assay.

Foci Reduction Neutralization Test (FRNT)

Cells and Viruses: Vero E6 cells expressing human transmembrane serine protease 2 (TMPRSS2; JCRB1819) were obtained from the Japanese Collection of Research Bioresources Cell Bank (Ibaraki City, Osaka, Japan) and grown at 37°C with 5% CO_2 in Dulbecco's modified eagle medium (DMEM) (Gibco, NY) supplemented with 10% fetal bovine serum (FBS) (R&D Systems, GA) and 100 µg/ml Geneticin G418 (Sigma Aldrich, MO). The SARS-CoV-2 USA_WA1/2020 stock (lineage A) was passaged five times in Vero E6 cells and screened by next generation sequencing to confirm its identity as well as lack of tissue culture adaptations or mycoplasma contamination.

Assay: Antibody neutralization was assessed by FRNT essentially as previously described (*79*). Mouse sera were heat-inactivated for 30 minutes at 56°C. Samples were serially 1:2 diluted in Dulbecco's phosphate buffered saline (DPBS) (Corning, VA) over a range spanning 1:10 to 1:2,560. These dilutions were performed with independent triplicates. Control wells, which contained DPBS with no antibody, were included in triplicate on each plate. An equal volume of SARS-CoV-2, diluted in DPBS to a concentration of $5x10^3$ focus forming units (FFU/ml), was combined with the diluted sera such that the final antibody dilution factor range spanned 1:20 to 1:5,120. The virus and antibody were incubated for 1 hour at 37°C with 5% CO_2 prior to 20 µL per well being transferred to 96-well plates with confluent monolayers of Vero E6 TMPRSS2 cells. The infection was allowed to proceed for 1 hour at 37°C prior to being overlaid with 85% minimum essential medium (Gibco) and 15% DMEM supplemented with 0.85% $^{w}/_{v}$ methylcellulose (Sigma Aldrich), 2% FBS, 100µg/ml Geneticin G418, and 1% antibiotic-antimycotic (Sigma Aldrich).

The assays were incubated at 37°C with 5% CO_2 for a further one day prior to fixation in 10% buffered formalin. Fixed monolayers were washed three times in DPBS before being incubated in permeabilization buffer (0.1% ^{w}/v each of BSA [Sigma] and saponin [Sigma] in DPBS) for 30 minutes at room temperature. This buffer was replaced with permeabilization buffer containing a 1:1,000 dilution of polyclonal rabbit anti-SARS-CoV nucleocapsid antibody and allowed to incubate at 4°C overnight. Unbound primary antibody was removed by three washes in DPBS, and HRP-linked goat anti-rabbit IgG (Cell Signaling, MA) diluted 1:2,000 in permeabilization buffer was added and allowed to bind for 1 hour at room temperature. The unbound secondary antibody was removed by three washes in DPBS, and KPL TrueBlue peroxidase substrate (SeraCare, MA) was added. The reaction was allowed to proceed until foci were visualized, at which time the substrate was removed and the plates rinsed with water. Images of each well were captured using the Cytation7 Imaging Reader (BioTek, VT), and foci were counted manually.

The percent reduction in foci was calculated in comparison to the average of the three control wells within each plate. This data was fitted using the [Agonist] vs. response – Find EC anything function of Prism with the following constraints: the bottom limit was set to 0, the top limit was set to 100, and the F was set to either 50 or 80 to calculate the EC_{50} or EC_{80} values, respectively.

Flow cytometry

Four weeks post-boost, both the immunized and the control hACE2-transgenic AC70 mice (n=5/group) were euthanized. Lungs from each mouse were infused with 10 ml PBS to remove residue blood. Spleen and lung tissues were then collected, and single-cell suspensions were made (*80, 81*). For B cell staining, about 2 million splenocytes from each spleen suspension were used. The cells were first blocked with anti-CD16/32 and then stained with Live/dead dye eFluor 780 and fluorescence-conjugated antibodies specific for memory B cells (Supplemental Table S1). For T cell staining, about 2 million splenocytes from both spleen and lung suspension were used. The cells were first seeded into a 96-well plate and stimulated with S-ecto or HA-stem trimers (60-100 µg/ml) for 16 hours at 37°C followed by incubation with Brefeldin A for an additional 4 hours. Cells were then harvested and stained with Live/dead dye eFlor780 and fluorescence-conjugated antibodies specific for various T cell surface markers (Supplemental Table S1). After washing with FACS buffer, cells were treated with eBioscience™ Foxp3 permeabilization buffer (Thermo Fisher) and stained for various cytokine markers (Supplemental Table S1). The differential cell populations were then acquired on flow cytometer (BD Symphony A5 SE, NJ) and analyzed with FlowJo software. The memory B cells and effector memory T cells from spleen tissue were identified as $CD19^{+}CD3^{-}CD138^{-}/CD38^{+}GL7^{-}/CD73^{+}CD80^{+}PDL2^{+}$ and $CD3^{+}/CD4^{+}$or $CD8^{+}/CD44^{+}CD62L^{-}CD127^{-}$, respectively. While Lung CD4 and CD8 T_{RM} were gated as $CD3^{+}CD4^{+}CD8^{-}CD44^{+}CD69^{+}$CD11a+ or $CD3^{+}CD8^{+}CD4^{-}CD44^{+}CD69^{+}Cd103^{+}CD49a^{+}$, respectively.

Photo credit

Mouse and virus images (Figs. 4A and 7A) were created using BioRender (BioRender.com). T4 structure and schematics were created using ChimeraX. The figure data were organized using Photoshop CS6 (Adobe, CA).

Statistical analysis

Statistical tests were performed using GraphPad Prism v9 software. For comparing multiple groups, one-way or two-way ANOVA with Tukey's post-*hoc* tests for multiple comparisons were used. A nonparametric Student's *t*-test was used to compare two groups. P values < 0.05 were considered significant. *, $P < 0.05$; **, $P < 0.01$; ***, $P < 0.001$; ****, $P < 0.0001$; ns, not significant. All data were presented as mean ± standard deviation (SD).

List of Supplementary Materials

Fig. S1 to S7

Table S1

Acknowledgments:

The authors thank Michell Brooke and Rachael Reyna for their help in performing FRNT. We thank Dr. Shinji Makino, UTMB, for providing polyclonal rabbit anti-SARS-CoV nucleocapsid antibodies for performing FRNT.

Funding: This research was supported by NIAID/NIH supplement grant 3R01AI095366-07S1 (sub-award 1100992-100) and in part by NIAID/NIH grants AI081726 and AI175340, NIDA/NIH Avant Garde Award DP1DA060580, and National Science Foundation grant MCB-0923873 to V.B.R. AKC was funded through the Sealy-Institute for Human Infection and Immunity (IHII) grant, UTMB, to perform these studies.

Author contributions: V.B.R., A.K.C., and J.Z. conceptualized and supervised the project. J.Z., J.S., H.B., S.J., X.W., E.K.H., P.B.K., and P.T. performed majority of experiments. K.S. isolated lung cells. K.S.P., J.A.P., and J.W. conducted FRNT assays. J.Z., V.B.R., J.S., and A.K.C analyzed and interpreted data and drafted the manuscript. All authors reviewed and edited the manuscript.

Competing interests: Authors declare that they have no competing interests.

Data and materials availability: All data are available in the main text or the supplementary materials.

Figures

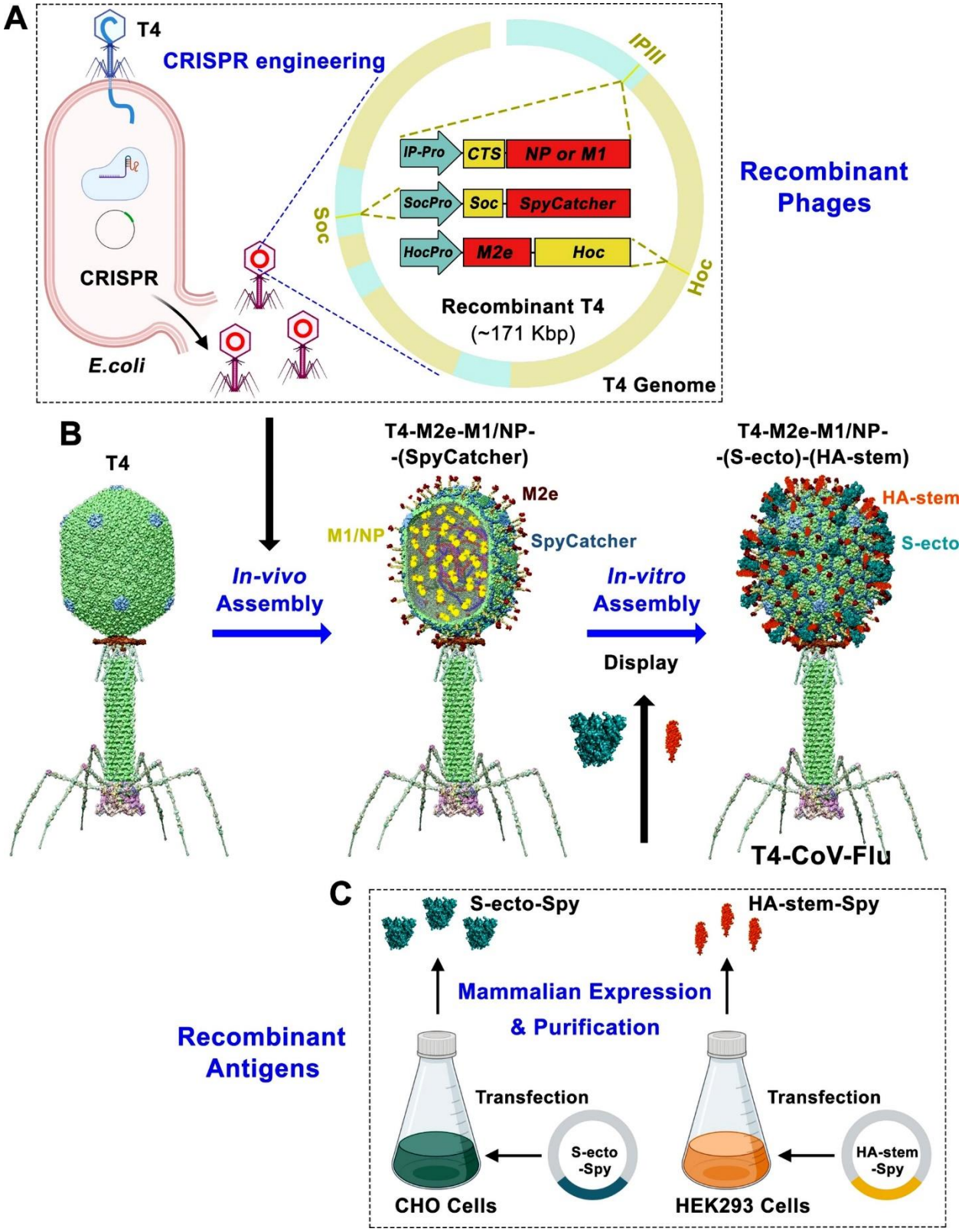

Fig. 1. A two-step strategy to design phage T4-CoV-Flu multivalent vaccine.

(A) CRISPR engineering of recombinant T4 phages displaying Flu-M1, Flu-M2e, CoV-NP, and SpyCatcher in *E. coli*. **(B)** Assembly of T4-CoV-Flu vaccine through *in vivo* antigen display and *in vitro* SpyCatcher-SpyTag conjugation of mammalian cell-expressed S-ecto and HA-stem trimers. **(C)** Production of S-ecto-Spy and HA-stem-Spy trimers in CHO and HEK293F cells for phage conjugation.

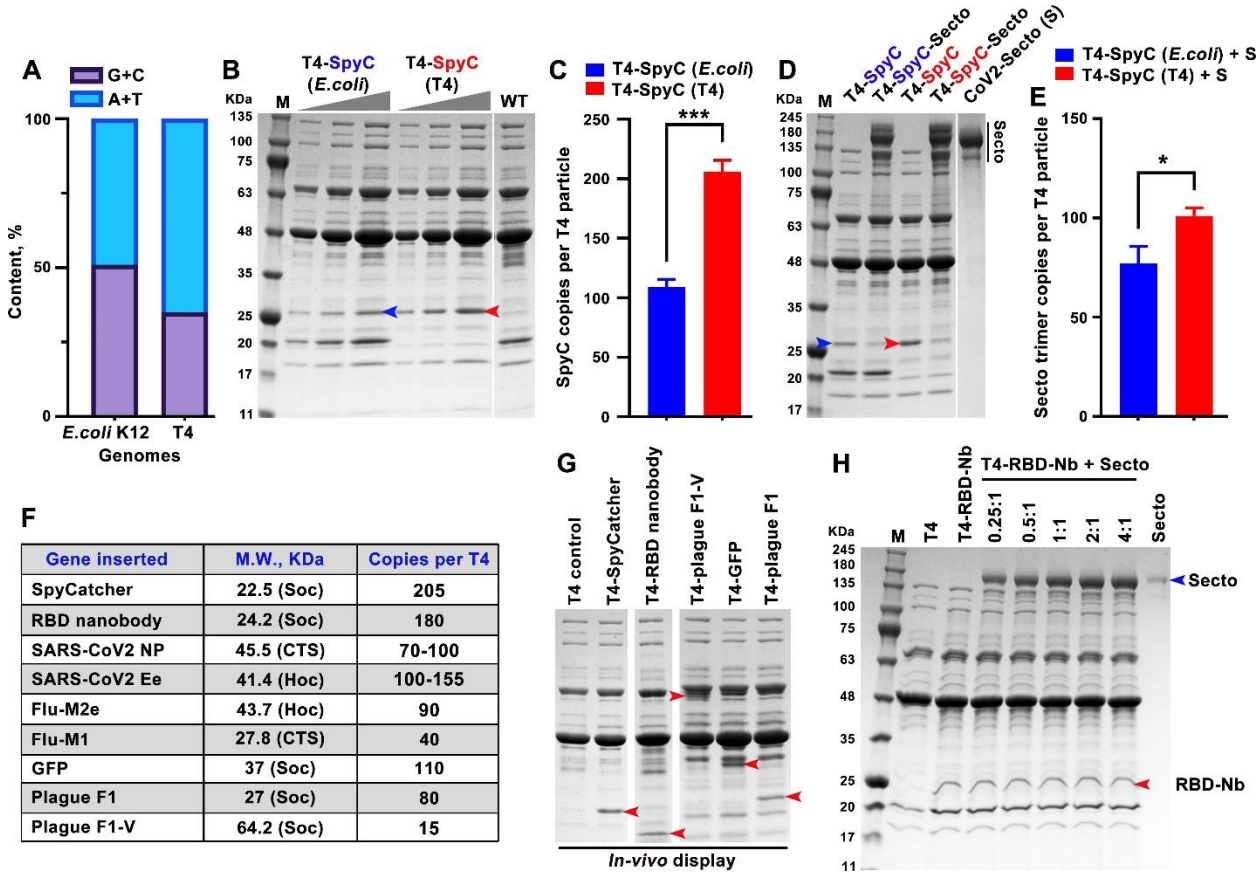

F

Gene inserted	M.W., KDa	Copies per T4
SpyCatcher	22.5 (Soc)	205
RBD nanobody	24.2 (Soc)	180
SARS-CoV2 NP	45.5 (CTS)	70-100
SARS-CoV2 Ee	41.4 (Hoc)	100-155
Flu-M2e	43.7 (Hoc)	90
Flu-M1	27.8 (CTS)	40
GFP	37 (Soc)	110
Plague F1	27 (Soc)	80
Plague F1-V	64.2 (Soc)	15

Fig. 2. Optimized *in vivo* display and encapsulation of multiple pathogen antigens into T4 nanoparticle. (A) Comparison of nucleotide content (A+T and G+C) in *E. coli* K12 and T4 genomes. **(B** and **C)** Comparison of display efficiency between *E. coli*-codon (blue) and T4-codon (red) optimized Soc-SpyCatcher (SpyC) by SDS–polyacrylamide gel electrophoresis (PAGE) (B) and quantitative analysis (C). The molecular weight standards (M) in KDa are shown on the left of the gel. **(D** and **E)** SDS-PAGE (D) and quantitative analysis (E) of Spy-tagged S-ecto trimers displayed on the T4 capsid. The interaction efficiency between S-ecto trimers and *E. coli*- or T4-codon-optimized SpyC was assessed, demonstrating improved display with T4-codon-optimized SpyC. **(F)** Table showing various antigens of interest either displayed on or encapsidated into the T4 capsid, their sizes, and copy numbers. **(G)** SDS-PAGE showing the display of representative proteins on the T4 capsid. Red arrowheads indicate the positions of the corresponding proteins. **(H)** SDS-PAGE showing display of S-ecto trimers on T4 capsid through S-ecto and RBD nanobody (RBD-Nb) interaction. The positions of S-ecto and RBD-Nb are indicated. A nonparametric Student's *t*-test was used to compare T4-SpyC (*E. coli*) versus T4-SpyC (T4) groups in (C) and (E). *, $P < 0.05$; ***, $P < 0.001$. Data represent means ± standard deviation (SD) from three replicates.

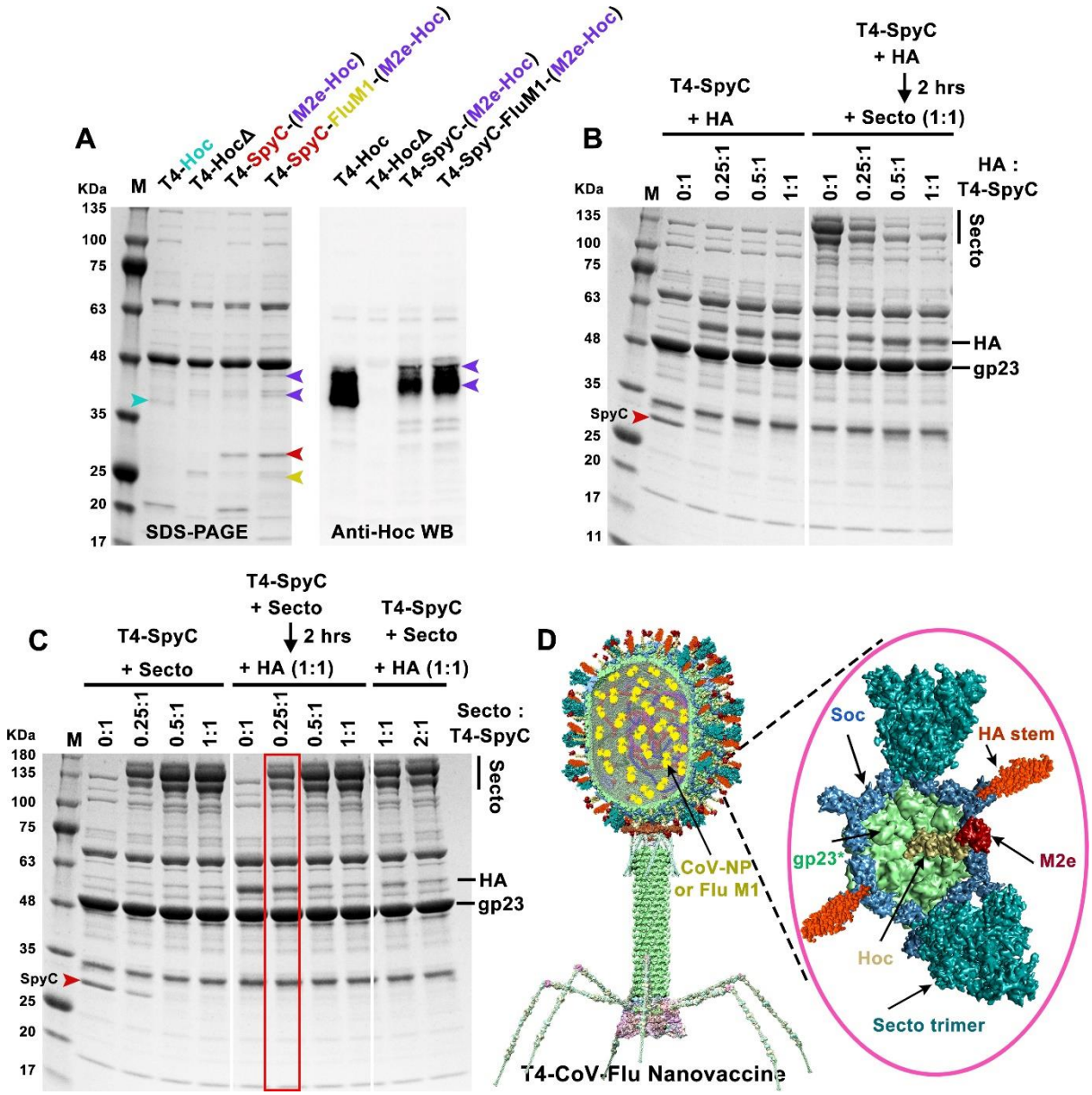

Fig. 3. **Assembly of the multivalent T4-CoV-Flu nanovaccine. (A)** SDS-PAGE and Western Blot (WB) analyses of phage nanoparticles displaying M2e and SpyC and encapsulating M1 *in vivo*. Note that due to the similar molecular size of Hoc and M2e-Hoc to other T4 structural proteins, a Hoc-specific antibody was used to detect Hoc and M2e-Hoc. Arrowheads with various colors indicate the corresponding displayed or encapsidated antigens. **(B** and **C)** Optimization of the co-display of S-ecto and HA-stem trimers. (B) *In vitro* display of HA stem trimers on T4-SpyC phage (left) and sequential co-display of HA stem and S-ecto trimers (HA added first, incubated, then S-ecto) (right) at increasing ratios of HA stem trimer molecules to Soc binding sites (0:1 to 1:1). The ratio of S-ecto trimer molecules to Soc binding sites was fixed at 1:1 in the co-display assay. (C) *In vitro* display of S-ecto trimers on T4-SpyC phage (left), sequential co-display of S-ecto and HA stem trimers (S-ecto added first, incubated, then HA) (middle), and simultaneous co-display of S-ecto and HA stem trimers (both added at the same time) (right) at increasing ratios of S-ecto trimer molecules to Soc binding sites (0:1 to 2:1). The ratio of HA stem trimer molecules to Soc binding sites was fixed at 1:1 in the co-display assay. **(D)** Structural model of the final T4-

CoV-Flu nanovaccine. Inset: Enlarged view of a single hexameric capsomer showing six subunits of major capsid protein gp23* (green) associated with trimers of Soc (blue) and Hoc fiber (yellow). The Flu M2e peptide (dark red) is displayed at the tips of Hoc fibers, while the SpyCatcher-Soc fusions surround the capsomer periphery. The CoV NP or Flu M1 molecules (yellow) are packaged inside the capsid. Spy-tagged S-ecto trimers (cyan) and HA stem trimers (red) are co-conjugated to Soc-SpyCatcher trimers.

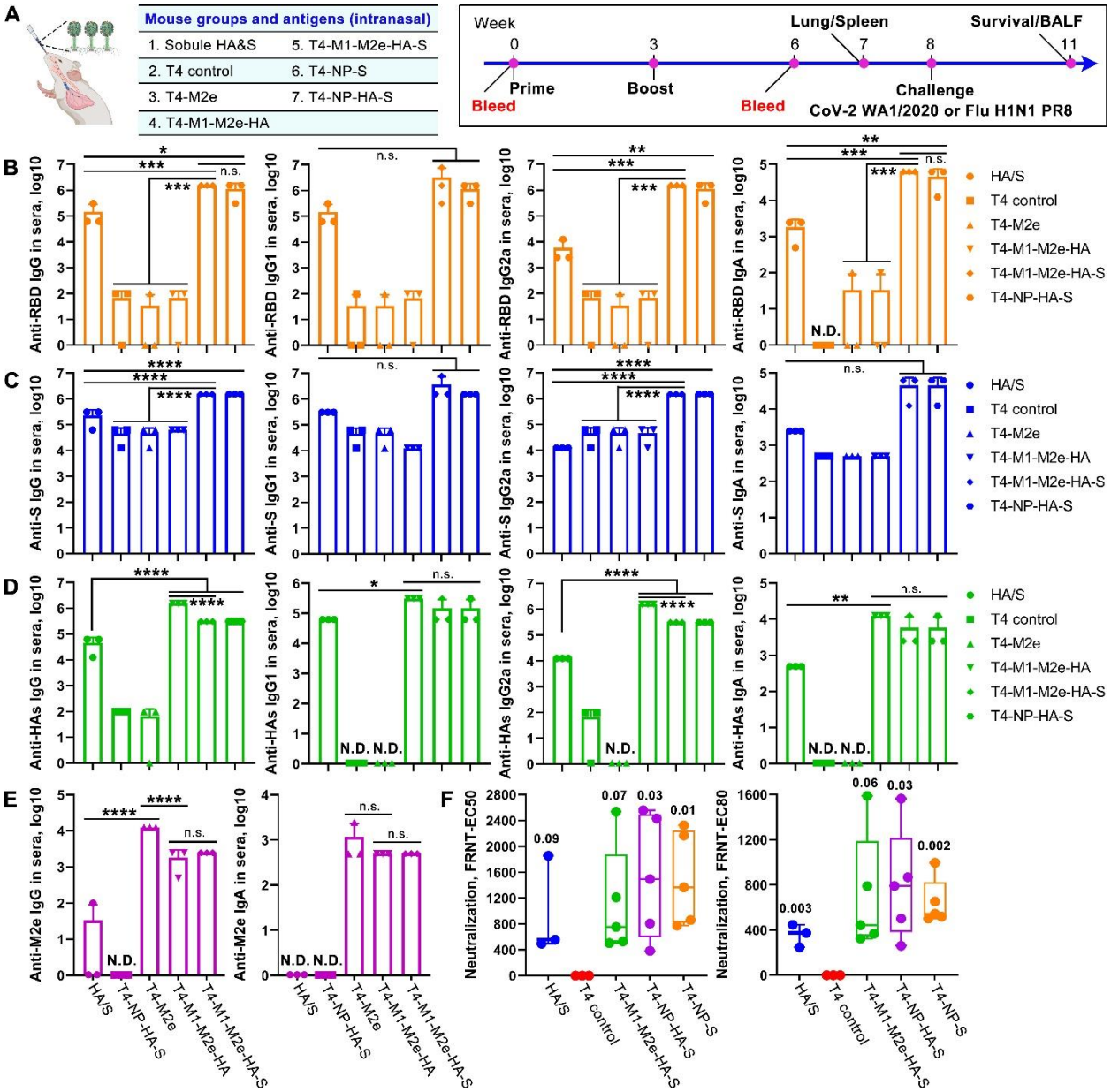

Fig. 4. Intranasal immunization with T4-CoV-Flu vaccine elicited strong systemic humoral immune responses against multiple SARS-CoV-2 and influenza antigens. (A) Schematic representation of intranasal mouse vaccinations with various T4-CoV-Flu vaccine candidates. **(B** to **E)** Antibody responses against SARS-CoV-2 and influenza antigens in the sera of immunized

BALB/c mice at day 21 post-final dose. ELISA was used to measure the reciprocal endpoint antibody titers for anti-RBD IgG/IgG1/IgG2a/IgA (B), anti-S-ecto IgG/IgG1/IgG2a/IgA (C), anti-HA IgG/IgG1/IgG2a/IgA (D), and anti-M2e IgG/IgA (E). **(F)** Serum neutralizing activity measured by Focus Reduction Neutralization Test (FRNT) assay using live SARS-CoV-2 US-WA-1/2020 strain. FRNT EC_{50} and EC_{80} values for individual serum samples from control and vaccine groups are shown. Data represent means ± SD from three pooled independent experiments (n=5). N.D. indicates not detected. Statistical comparisons among multiple groups in (B) to (E) were made using one-way analysis of variance (ANOVA) with Tukey's post *hoc* test. *, $P < 0.05$; **, $P < 0.01$; ***, $P < 0.001$; ****, $P < 0.0001$; n.s., not significant. In (F), Student's *t*-test was applied to compare HA/S and T4 CoV-Flu vaccine groups with T4 control. *P* values are indicated.

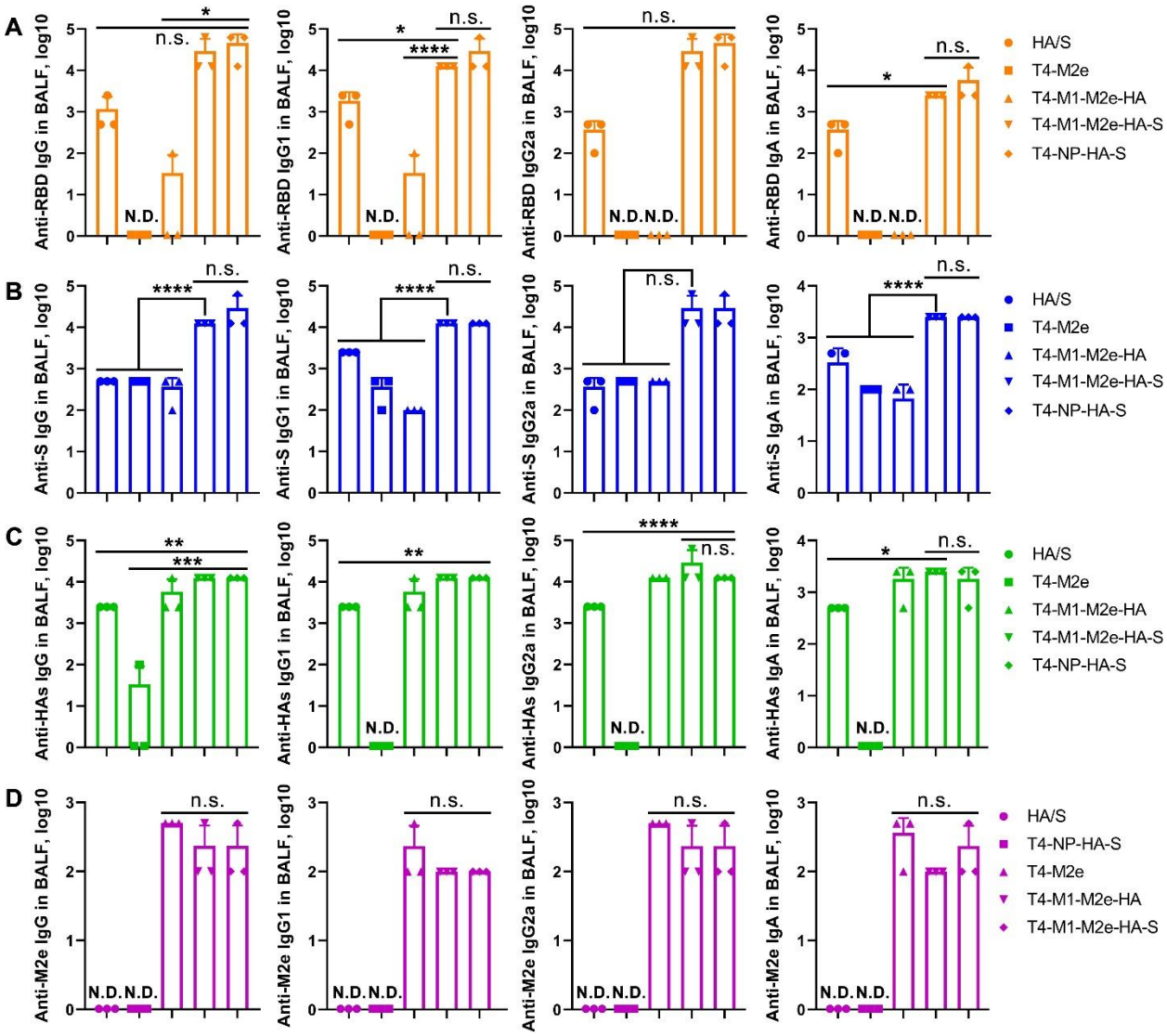

Fig. 5. The T4-CoV-Flu intranasal vaccine induced robust mucosal humoral immune responses. The reciprocal endpoint antibody titers in BALF of anti-RBD IgG/IgG1/IgG2a/IgA **(A)**, anti-S-ecto IgG/IgG1/IgG2a/IgA **(B)**, anti-HA IgG/IgG1/IgG2a/IgA **(C)**, and anti-M2e IgG/IgG1/IgG2a/IgA **(D)** are shown. Data represent means ± SD. N.D., not detected. The data are from three pooled independent experiments (n=5). Statistical comparisons among multiple

groups were made using one-way ANOVA with Tukey's post *hoc* test. *, $P < 0.05$; **, $P < 0.01$; ***, $P < 0.001$; ****, $P < 0.0001$; n.s., not significant.

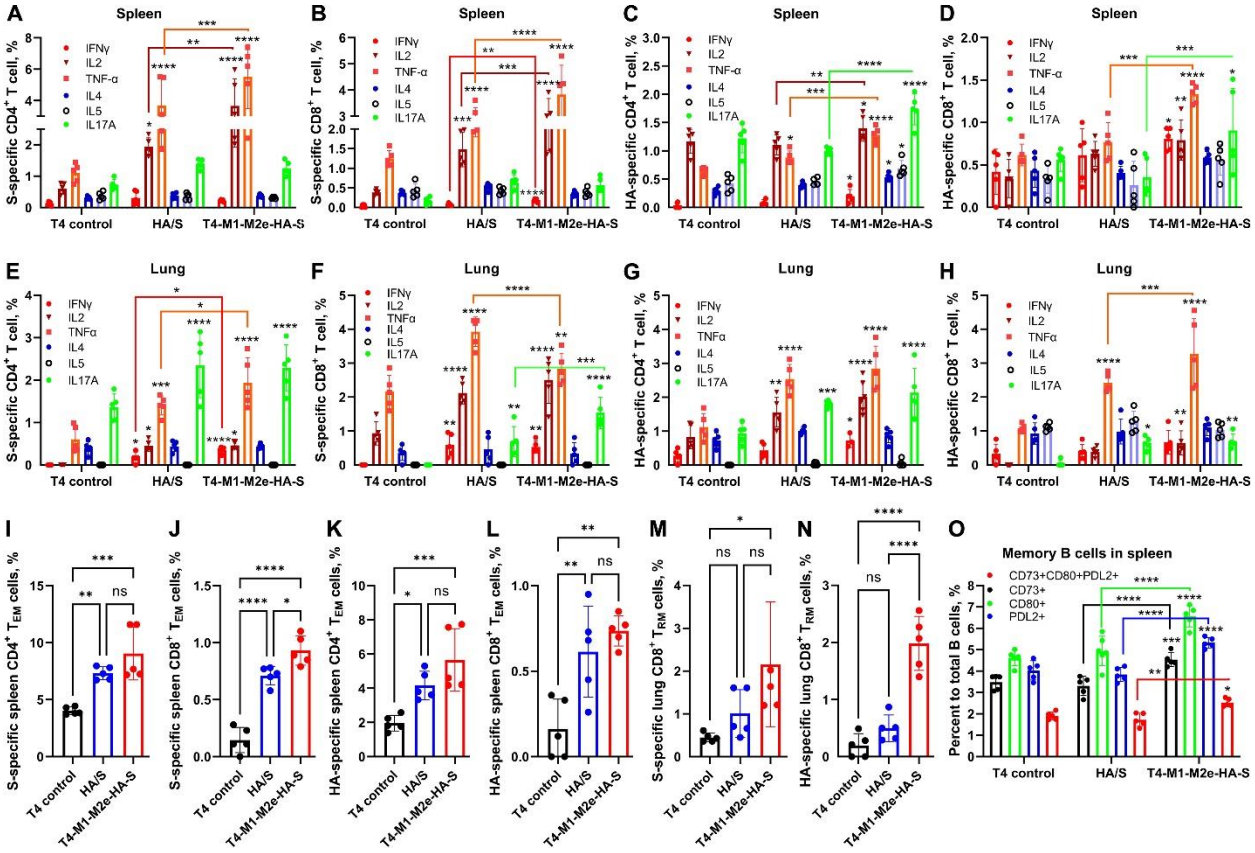

Fig. 6. **The T4-CoV-Flu intranasal vaccine elicits strong systemic and mucosal cellular immune responses.** Mice immunized with T4 vector control, soluble HA-stem and S-ecto trimers (HA/S-trimer), or phage expressing HA-stem and S-ecto trimers (T4-M1-M2e-HA-S) were compared. Lungs and spleens were harvested after immunization and single-cell suspensions were prepared. Cells were stimulated with 100 µg/ml of either SARS-CoV-2 S-trimers or H1N1 HA-stem trimers for 16 hours, followed by an additional 4-hour incubation with Brefeldin A. Cells were then harvested and stained for various surface markers and cytokines. For T effector memory (T_{EM}) cells: $CD44^+CD62L^-CD127^-$. For lung $CD8^+$ tissue-resident memory T cells ($CD8^+$ T_{RM}): $CD8^+CD4^-CD44^+CD69^+CD103^+CD49a^+$. For lung $CD4^+$ T_{RM}: $CD4^+CD8^-$ $CD44^+CD69^+CD11a^+$. For memory B cells, splenocytes were directly stained without stimulation for the phenotype: $CD19^+CD3^-CD138^-/CD38^+GL7^-/CD73^+CD80^+PDL2^+$. The percentages of these cells were plotted and compared among T4 control, soluble HA/S-trimer, and T4-M1-M2e-HA-S groups. **(A to D)** The percentages of S-ecto-specific $CD4^+$ T cells (A) and $CD8^+$ T cells (B), and HA-specific $CD4^+$ T cells (C) and $CD8^+$ T cells (D) secreting various cytokines (IFNγ, IL2, TNFα, IL4, IL5, and IL17A) in the splenocytes. **(E to H)** The percentages of S-ecto-specific $CD4^+$ T cells (E) and $CD8^+$ T cells (F), and HA-specific $CD4^+$ T cells (G) and $CD8^+$ T cells (H) secreting various cytokines (IFNγ, IL2, TNFα, IL4, IL5, and IL17A) in the lung. **(I** to **L)** The percentages of S-ecto-specific $CD4^+$ T_{EM} cells (I) and $CD8^+$ T_{EM} cells (J), and HA-specific $CD4^+$ T_{EM} cells (K) and $CD8^+$ T_{EM} cells (L) in the splenocytes. **(M** and **N)** The percentages of S-ecto-specific $CD8^+$ T_{RM} (M) and HA-specific $CD8^+$ T_{RM} (N) in the lung. **(O)** The percentages of memory B cells to total B cells in the splenocytes. Data represent means ± SD (n=5). Statistical comparisons among multiple

groups were made using two-way ANOVA with Tukey's post *hoc* test in (A to H) and (O). One-way ANOVA with Tukey's multiple comparisons test was used to analyze statistical significance in (I to N). *, $P < 0.05$; **, $P < 0.01$; ***, $P < 0.001$; ****, $P < 0.0001$; ns, not significant.

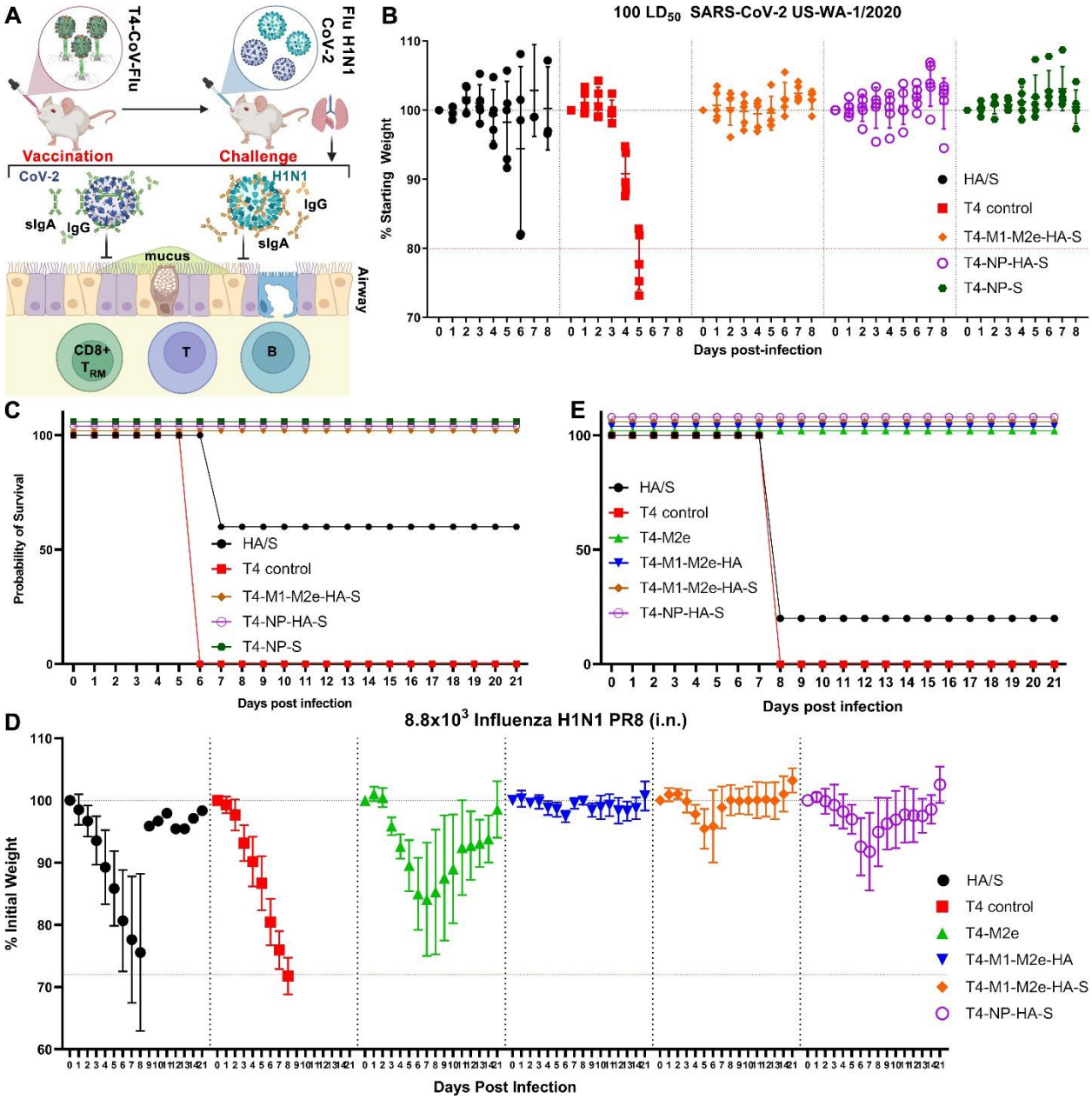

Fig. 7. **The T4-CoV-Flu intranasal vaccine conferred complete protection against high-dose SARS-CoV-2 and H1N1 challenges. (A)** Schematic of T4-CoV-Flu intranasal vaccine protection against SARS-CoV-2 and influenza challenge through mouse airways. **(B** and **C)** Evaluation of the protective efficacy of T4-CoV-Flu vaccine candidates against SARS-CoV-2 in mice. (B) Percent starting body weight of immunized mice over days following intranasal challenge with 100 LD_{50} SARS-CoV-2 US-WA-1/2020. (C) Survival rate of mice following the SARS-CoV-2 challenge. **(D and E)** Assessment of the protective efficacy of T4-CoV-Flu vaccine candidates against influenza challenge. (D) Percent change in body weight of immunized mice over time after

intranasal challenge with 8.8 x 10^3 influenza H1N1 PR8. (E) Survival rate of mice following H1N1 PR8 challenge. The data are presented as means ± SD (n=5).

Supplemental Figures and Tables

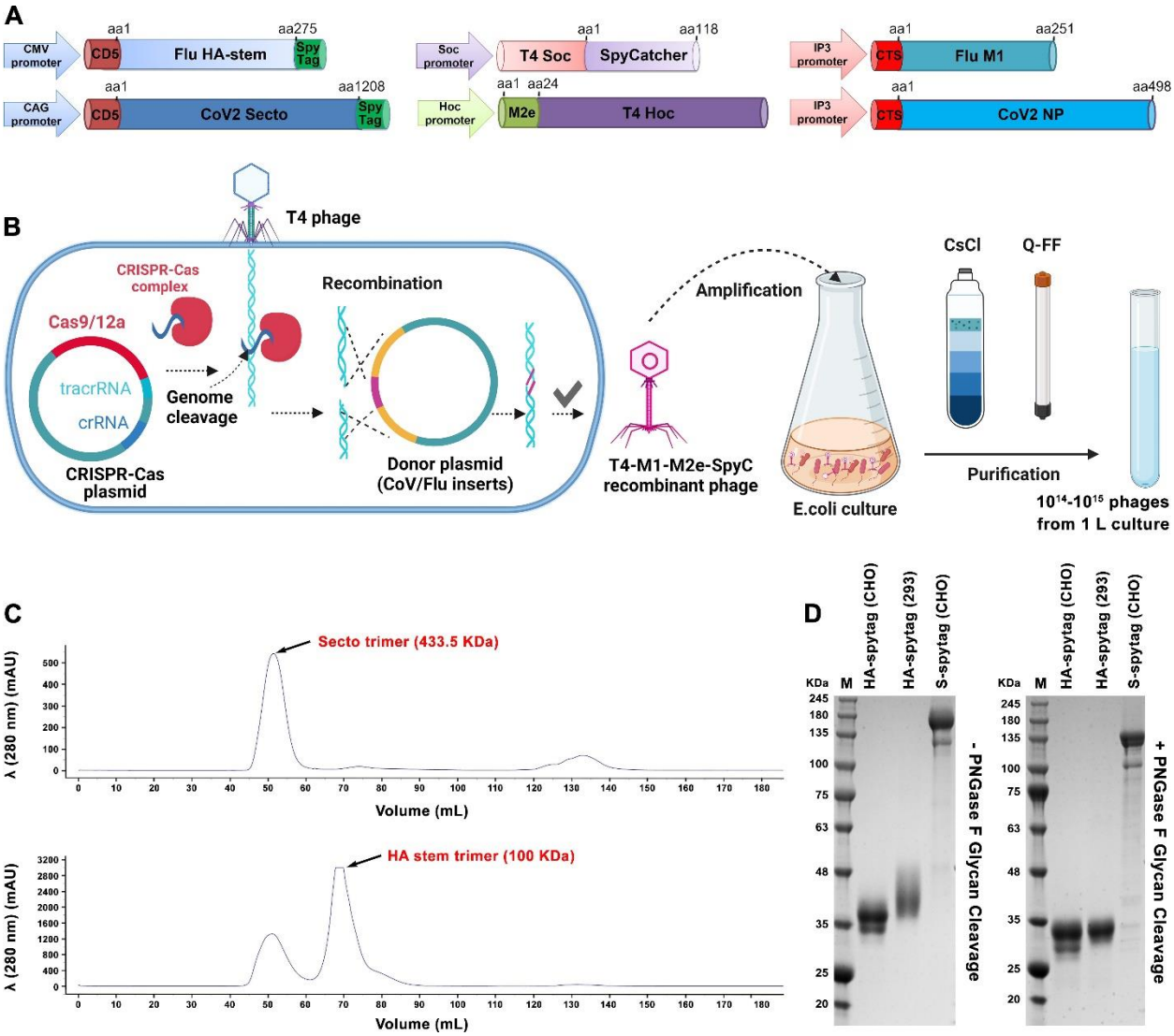

Fig. S1. Components of the T4-CoV-Flu nanovaccine. (A) Schematic of various gene expression cassettes for T4 *in vitro* display, *in vivo* display, and encapsidation. **(B)** Schematic of CRISPR engineering scheme for the production of recombinant T4-M1-M2e-SpyCatcher phage. **(C** and **D)** Purification and characterization of S-ecto-Spytag trimers from ExpiCHO cells and HA stem-Spytag trimers from HEK293F cells. (C) Size-exclusion chromatography (SEC) elution profiles of S-ecto-Spytag trimers (top) and HA stem trimers (bottom). (D) SDS-PAGE patterns of SEC-purified HA stem-Spytag trimers (from ExpiCHO or HEK293F cells) and S-ecto-Spytag trimers (from ExpiCHO), both without (left) and with (right) the treatment of PNGase F glycan cleavage enzyme. Note the band shift of the envelope proteins following deglycosylation. The molecular weight standards (M) in KDa are shown on the left of each gel.

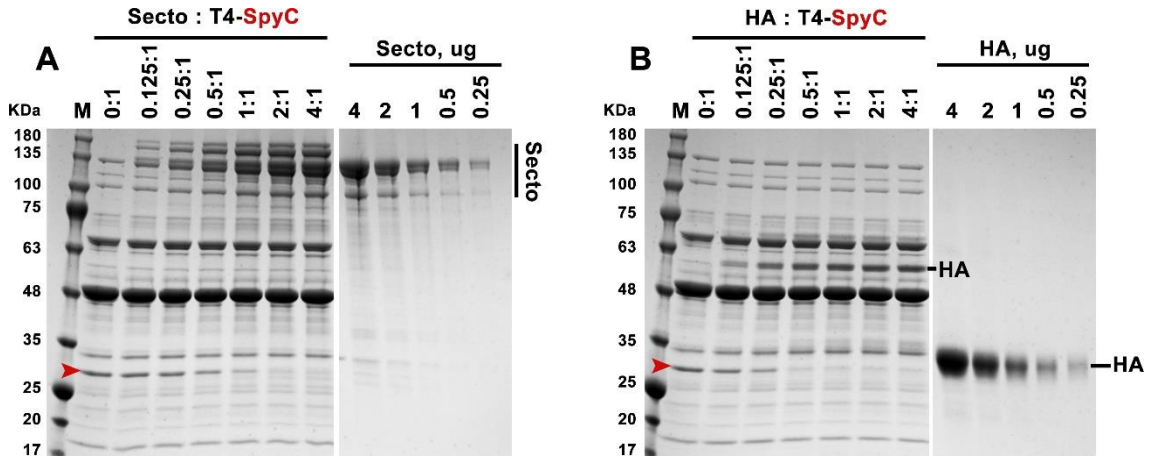

Fig. S2. Optimization of S-ecto and HA-stem trimer display on T4 capsid. (A) *In vitro* display of S-ecto trimers on T4-SpyC phage at increasing ratios of S-ecto trimer molecules to Soc binding sites (0:1 to 4:1). S-ecto standard was used for quantification. **(B)** *In vitro* display of HA stem trimers on T4-SpyC phage at increasing ratios of HA stem trimer molecules to Soc binding sites (0:1 to 4:1). HA standard was used for quantification. Arrowheads depict the position of the Soc-SpyCatcher band which reduces in intensity as it gets conjugated with SpyTagged trimers with increasing SpyTagged trimers to Soc-SpyCatcher ratios.

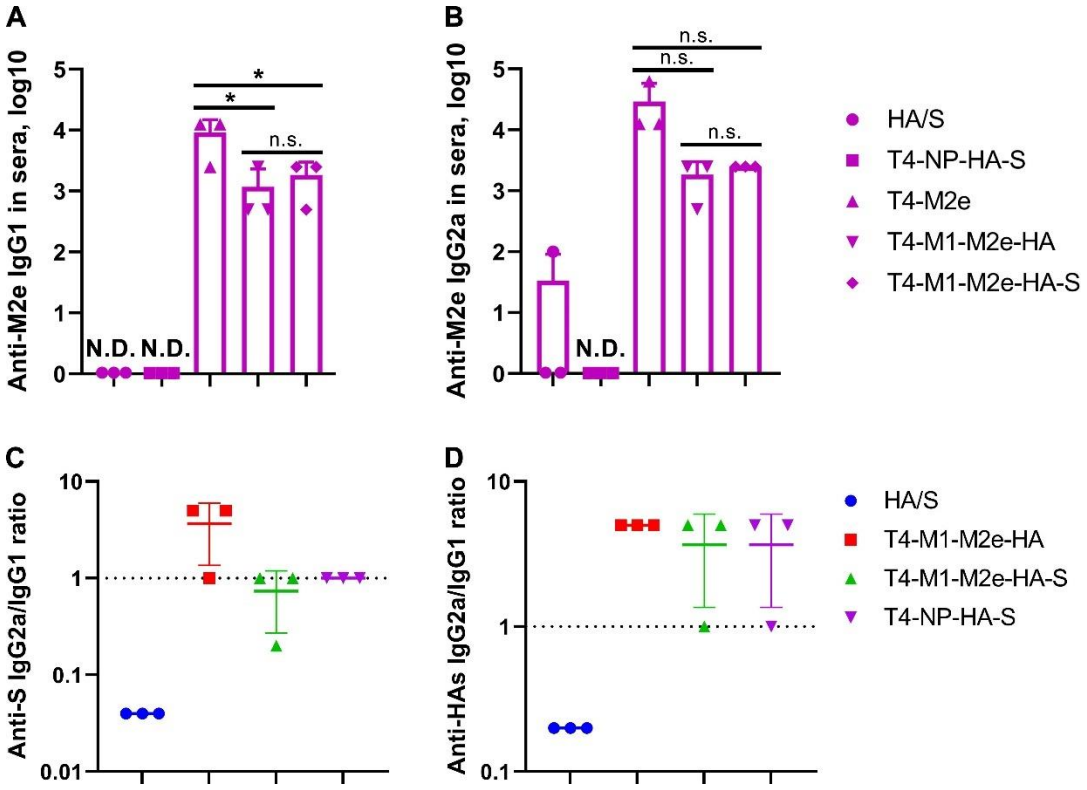

Fig. S3. **Intranasal immunization with T4-CoV-Flu vaccine elicited balanced systemic humoral immune responses. (A** and **B)** Anti-M2e IgG1/IgG2a antibody responses in the sera of immunized BALB/c mice. **(C** and **D**) Comparison of IgG2a/IgG1 ratios for S-ecto-specific (C) and HA-stem-specific (D) antibodies in mouse sera across HA/S and various T4-CoV-Flu groups.

The data are presented as means ± SD (n=3). Statistical comparisons among multiple groups were made using one-way analysis of variance (ANOVA) with Tukey's post *hoc* test. *, $P < 0.05$; n.s., not significant.

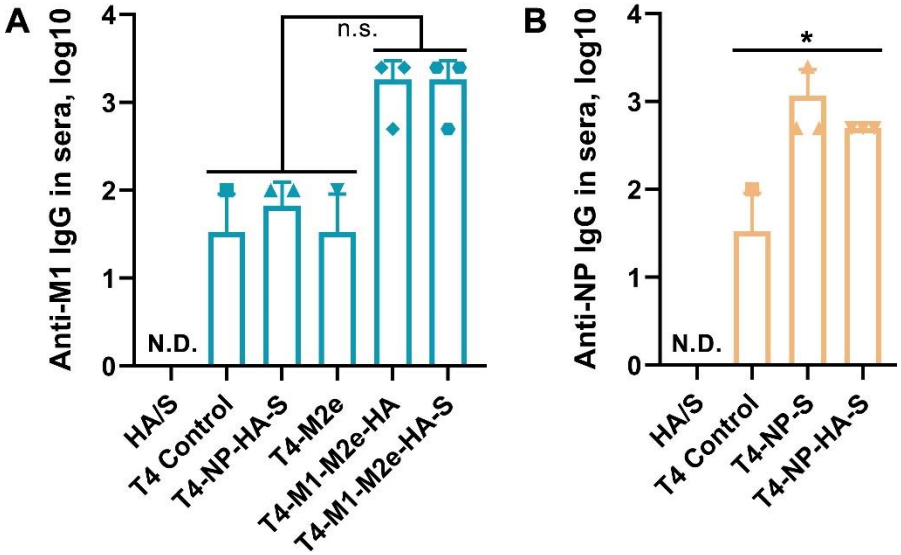

Fig. S4. **IgG antibody responses against M1 and NP in the sera of immunized mice. (A)** Anti-Flu M1 IgG in BALB/c mice sera. **(B)** Anti-CoV NP IgG in ACE2 transgenic mice sera. ELISA was used to measure the reciprocal endpoint antibody titers. Data represent means ± SD. N.D. indicates not detected. The data are from three pooled independent experiments (n=5). Statistical comparisons among multiple groups were made using one-way ANOVA with Tukey's post *hoc* test. *, $P < 0.05$; n.s., not significant.

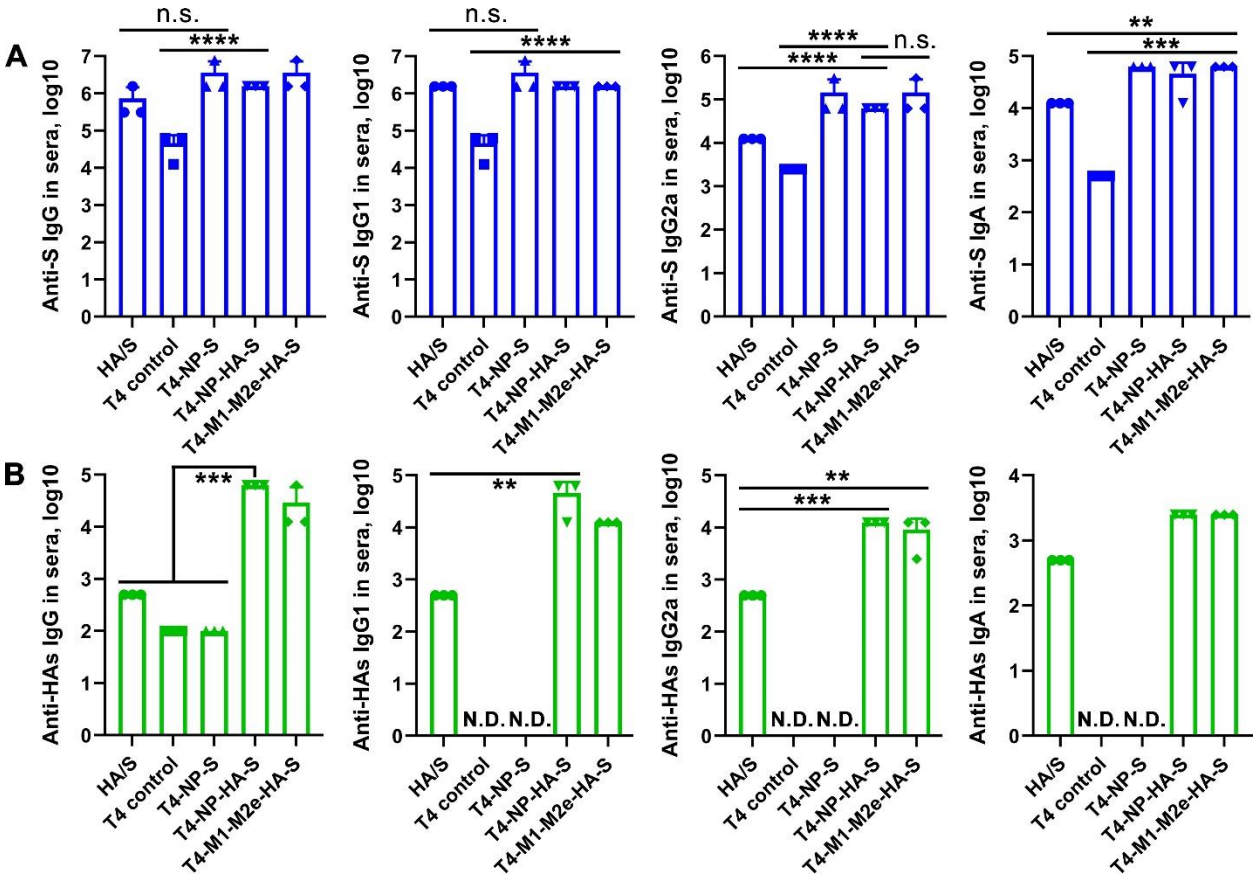

Fig. S5. **Antibody responses against CoV S-ecto and influenza HA-stem antigens in the sera of immunized hACE2 transgenic mice.** ELISA was used to measure the reciprocal endpoint antibody titers for anti-S-ecto IgG/IgG1/IgG2a/IgA **(A)** and anti-HA-stem IgG/IgG1/IgG2a/IgA **(B)**. Data represent means ± SD. N.D. indicates not detected. The data are from three pooled independent experiments (n=5). Statistical comparisons among multiple groups were made using one-way ANOVA with Tukey's post *hoc* test. **, $P < 0.01$; ***, $P < 0.001$; ****, $P < 0.0001$; n.s., not significant.

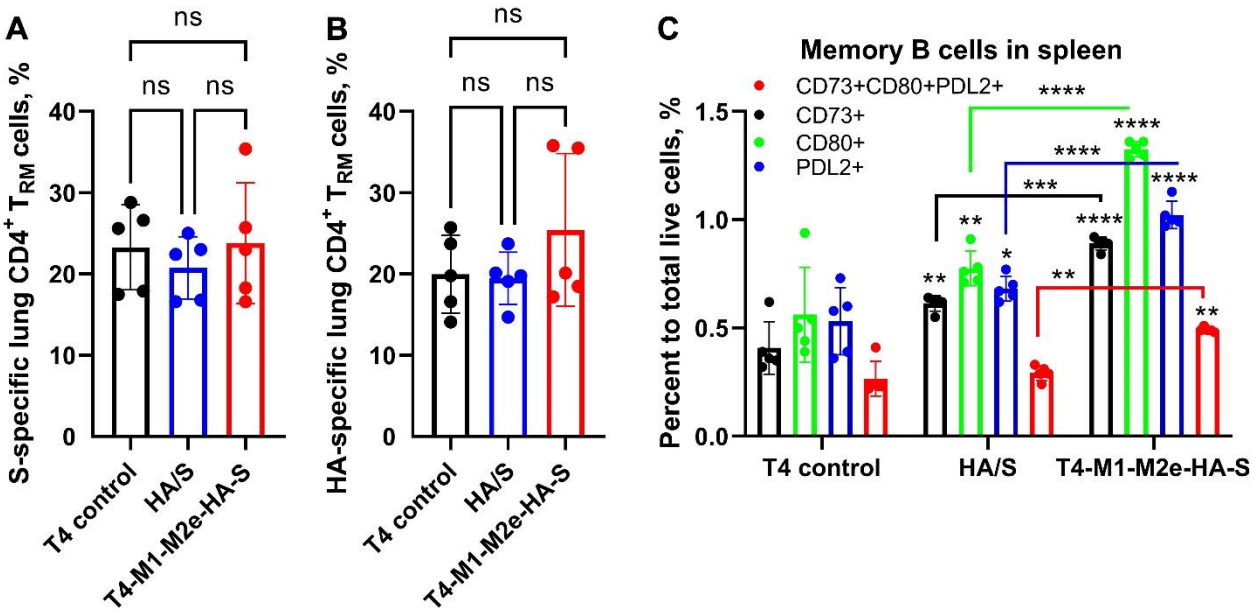

Fig. S6. **Comparison of memory B cells in spleen and CD4⁺ T_{RM} Cells in the lung among T4 control, soluble HA/S trimer, and T4-M1-M2e-HA-S groups. (A** and **B)** The percentages of S-ecto-specific CD4⁺ T_{RM} (A) and HA-specific CD4⁺ T_{RM} (B) in the lung. **(C)** The percentages of memory B cells among total live cells in the splenocytes. Data represent means ± SD (n=5). One-way ANOVA with Tukey's multiple comparisons test was used to analyze statistical significance in (A and B). Statistical comparisons among multiple groups were made using two-way ANOVA with Tukey's post *hoc* test in (C). *, $P < 0.05$; **, $P < 0.01$; ***, $P < 0.001$; ****, $P < 0.0001$; ns, not significant.

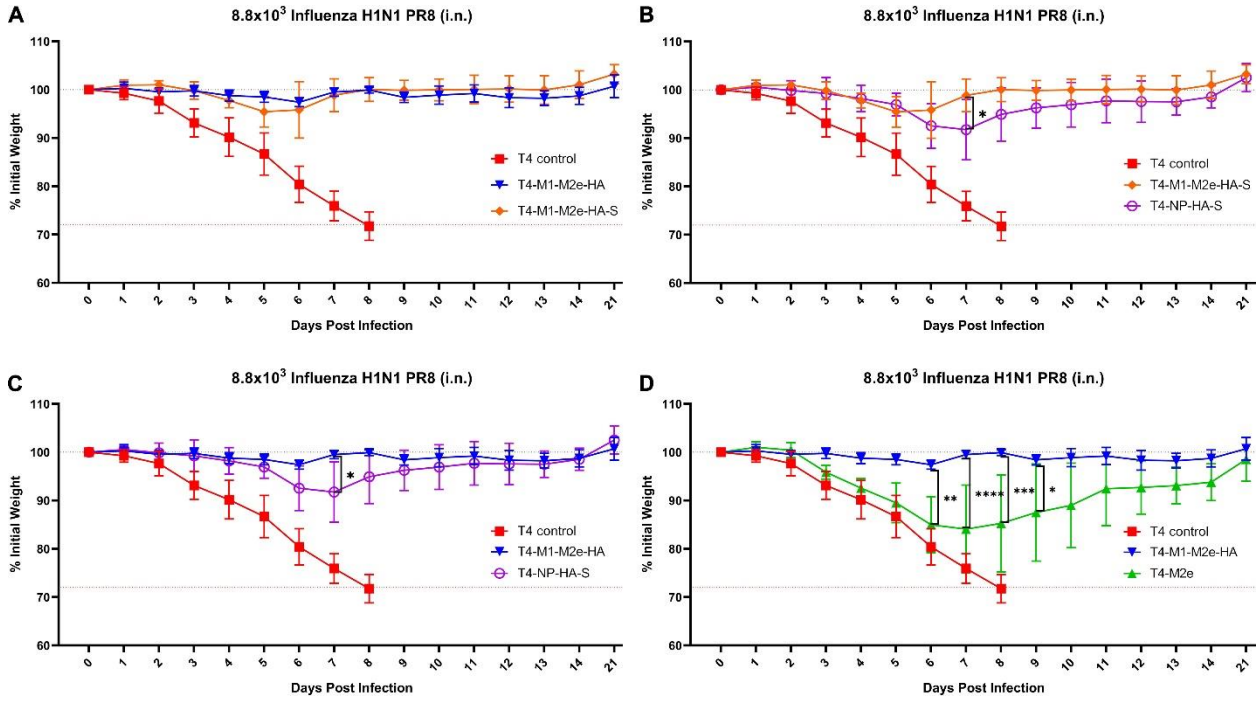

Fig. S7. **Body weight changes in T4-CoV-Flu intranasally-immunized mice following challenge with 8.8 x 10^3 Influenza H1N1 PR8.** Comparisons of body weights are shown: **(A)** Among T4 control, T4-MA-M2e-HA, and T4-M1-M2e-HA-S groups. **(B)** Among T4 control, T4-M1-M2e-HA-S, and T4-NP-HA-S groups. **(C)** Among T4 control, T4-M1-M2e-HA, and T4-NP-HA-S groups. **(D)** Among T4 control, T4-M1-M2e-HA, and T4-M2e groups. Data represent means ± SD (n=5). Statistical comparisons among multiple groups were made using two-way ANOVA with Tukey's post *hoc* test. *, $P < 0.05$; **, $P < 0.01$; ***, $P < 0.001$; ****, $P < 0.0001$.

Antibodies used for memory B cells				
Markers	Fluorophore	Clone	Vendor	Catalogue
CD19	FITC	6D5	BioLegend	115506
CD3	Alexa Fluor® 700	17A2	BioLegend	100216
CD138	BV650	281-2	Beckton Dickenson	564068
CD38	PE-Cy7	90	BioLegend	102718
GL7	Percp-cy5.5	GL7	BioLegend	144610
IgD	BV510	11-26c.a2	BioLegend	405723
CD80	BV421	16-10A1	BioLegend	104726
CD73	BV605	TY/11.8	BioLegend	127215
PDL2	PE	TY25	BioLegend	107206
Antibodies used for T cell surface staining				
CD3	Alexa Fluor® 700	17A2	BioLegend	100216
CD4	Brilliant Violet 785	GK1.5	BioLegend	100453
CD8	FITC	53-5.8	BioLegend	140403
CD44	BV510	IM7	BioLegend	103044
CD62L	BV711	MEL-14	BioLegend	104445
CD127	PE	S18006K	BioLegend	158204
CD69	BUV737	H1.2F3	BD Biosciences	612793
CD103	BUV395	M290	BD Biosciences	740238
CD49a	BV750	Hα31/8	BD Biosciences	746854
CD11a	BUV805	2D7	BD Biosciences	741919
Antibodies used for T cell intracellular staining				
IFN-γ	PerCP/Cyanine5.5	XMG1.2	Biolegend	505822
IL-2	PE-CF594	JES6-5H4	BD Biosciences	562483
TNF-α	eFluor 450	MP6-XT22	Thermo Fisher	48-7321-82
IL-4	BV650	11B11	BD Biosciences	564004
IL-5	APC	TRFK5	BD Biosciences	554396
IL-17A	PE/Cyanine7	TC11-18H10.1	Biolegend	506922

Table S1. Antibodies used for Flowcytometry

References and Notes

1. A. D. Iuliano *et al.*, Estimates of global seasonal influenza-associated respiratory mortality: a modelling study. *The Lancet* **391**, 1285-1300 (2018).
2. E. Cuadrado-Payán *et al.*, SARS-CoV-2 and influenza virus co-infection. *The Lancet* **395**, e84 (2020).
3. Y. Cheng *et al.*, Co-infection of influenza A virus and SARS-CoV-2: A retrospective cohort study. *J. Med. Virol.* **93**, 2947-2954 (2021).
4. S. A. Hashemi, S. Safamanesh, H. Ghasemzadeh-Moghaddam, M. Ghafouri, A. Azimian, High prevalence of SARS-CoV-2 and influenza A virus (H1N1) coinfection in dead patients in Northeastern Iran. *J. Med. Virol.* **93**, 1008-1012 (2021).
5. L. Bai *et al.*, Coinfection with influenza A virus enhances SARS-CoV-2 infectivity. *Cell Res.* **31**, 395-403 (2021).
6. P. Polack Fernando *et al.*, Safety and Efficacy of the BNT162b2 mRNA Covid-19 Vaccine. *N. Engl. J. Med.* **383**, 2603-2615 (2020).
7. J. Sadoff *et al.*, Safety and Efficacy of Single-Dose Ad26.COV2.S Vaccine against Covid-19. *N. Engl. J. Med.* **384**, 2187-2201 (2021).
8. A. M. Carabelli *et al.*, SARS-CoV-2 variant biology: immune escape, transmission and fitness. *Nat. Rev. Microbiol.* **21**, 162-177 (2023).
9. D. M. Altmann, R. J. Boyton, COVID-19 vaccination: The road ahead. *Science* **375**, 1127-1132 (2022).
10. S. Cele *et al.*, Omicron extensively but incompletely escapes Pfizer BNT162b2 neutralization. *Nature* **602**, 654-656 (2022).
11. E. J. Topol, A. Iwasaki, Operation Nasal Vaccine—Lightning speed to counter COVID-19. *Sci. Immunol.* **7**, eadd9947 (2022).
12. J. Tang *et al.*, Respiratory mucosal immunity against SARS-CoV-2 after mRNA vaccination. *Sci. Immunol.* **7**, eadd4853 (2022).
13. A. Singanayagam *et al.*, Community transmission and viral load kinetics of the SARS-CoV-2 delta (B.1.617.2) variant in vaccinated and unvaccinated individuals in the UK: a prospective, longitudinal, cohort study. *Lancet Infect. Dis.* **22**, 183-195 (2022).
14. S. Yamayoshi, Y. Kawaoka, Current and future influenza vaccines. *Nat. Med.* **25**, 212-220 (2019).
15. C. J. Wei *et al.*, Next-generation influenza vaccines: opportunities and challenges. *Nat. Rev. Drug Discov.* **19**, 239-252 (2020).
16. J. Guo *et al.*, Real-world effectiveness of seasonal influenza vaccination and age as effect modifier: A systematic review, meta-analysis and meta-regression of test-negative design studies. *Vaccine* **42**, 1883-1891 (2024).
17. N. Langel Stephanie *et al.*, Adenovirus type 5 SARS-CoV-2 vaccines delivered orally or intranasally reduced disease severity and transmission in a hamster model. *Sci. Transl. Med.* **14**, eabn6868 (2022).
18. T. Mao *et al.*, Unadjuvanted intranasal spike vaccine elicits protective mucosal immunity against sarbecoviruses. *Science* **378**, eabo2523 (2022).
19. A. O. Hassan *et al.*, A Single-Dose Intranasal ChAd Vaccine Protects Upper and Lower Respiratory Tracts against SARS-CoV-2. *Cell* **183**, 169-184 e113 (2020).
20. S. Afkhami *et al.*, Respiratory mucosal delivery of next-generation COVID-19 vaccine provides robust protection against both ancestral and variant strains of SARS-CoV-2. *Cell* **185**, 896-915 e19 (2022).
21. A. O. Hassan *et al.*, An intranasal vaccine durably protects against SARS-CoV-2 variants in mice. *Cell Rep.* **36**, 109452 (2021).

946 22. N. van Doremalen *et al.*, Intranasal ChAdOx1 nCoV-19/AZD1222 vaccination reduces viral
947 shedding after SARS-CoV-2 D614G challenge in preclinical models. *Sci. Transl. Med.* **13**, eabh0755
948 (2021).
949 23. T. Carvalho, Intranasal COVID-19 vaccine fails to induce mucosal immunity. *Nat. Med.* **28**, 2439-
950 2440 (2022).
951 24. E. Waltz, How nasal-spray vaccines could change the pandemic. *Nature* **609**, 240-242 (2022).
952 25. N. J. Carter, M. P. Curran, Live Attenuated Influenza Vaccine (FluMist®; Fluenz™): a review of its
953 use in the prevention of seasonal influenza in children and adults. *Drugs* **71**, 1591-1622 (2011).
954 26. S. Chivukula *et al.*, Development of multivalent mRNA vaccine candidates for seasonal or
955 pandemic influenza. *NPJ Vaccines* **6**, 153 (2021).
956 27. R. L. Hajnik *et al.*, Dual spike and nucleocapsid mRNA vaccination confer protection against SARS-
957 CoV-2 Omicron and Delta variants in preclinical models. *Sci. Transl. Med.* **14**, eabq1945 (2022).
958 28. M. O. Mohsen, M. F. Bachmann, Virus-like particle vaccinology, from bench to bedside. *Cell. Mol.*
959 *Immunol.* **19**, 993-1011 (2022).
960 29. S. Ols *et al.*, Multivalent antigen display on nanoparticle immunogens increases B cell clonotype
961 diversity and neutralization breadth to pneumoviruses. *Immunity*, **56**, 2425-2441.e14 (2023).
962 30. Y. Kato *et al.*, Multifaceted Effects of Antigen Valency on B Cell Response Composition and
963 Differentiation *In Vivo*. *Immunity* **53**, 548-563.e548 (2020).
964 31. J. Marcandalli *et al.*, Induction of Potent Neutralizing Antibody Responses by a Designed Protein
965 Nanoparticle Vaccine for Respiratory Syncytial Virus. *Cell* **176**, 1420-1431.e1417 (2019).
966 32. M. Kanekiyo *et al.*, Mosaic nanoparticle display of diverse influenza virus hemagglutinins elicits
967 broad B cell responses. *Nat. Immunol.* **20**, 362-372 (2019).
968 33. M. Kanekiyo *et al.*, Self-assembling influenza nanoparticle vaccines elicit broadly neutralizing
969 H1N1 antibodies. *Nature* **499**, 102-106 (2013).
970 34. J. Zhu, P. Tao, A. K. Chopra, V. B. Rao, Bacteriophage T4 as a Protein-Based, Adjuvant- and Needle-
971 Free, Mucosal Pandemic Vaccine Design Platform. *Annu. Rev. Virol.* **11**, 395-420 (2024).
972 35. Z. Chen *et al.*, Cryo-EM structure of the bacteriophage T4 isometric head at 3.3-A resolution and
973 its relevance to the assembly of icosahedral viruses. *Proc. Natl. Acad. Sci. U.S.A.* **114**, E8184-E8193
974 (2017).
975 36. P. Tao, J. Zhu, M. Mahalingam, H. Batra, V. B. Rao, Bacteriophage T4 nanoparticles for vaccine
976 delivery against infectious diseases. *Adv. Drug Deliv. Rev.* **145**, 57-72 (2019).
977 37. L. Qin, A. Fokine, E. O'Donnell, V. B. Rao, M. G. Rossmann, Structure of the small outer capsid
978 protein, Soc: a clamp for stabilizing capsids of T4-like phages. *J. Mol. Biol.* **395**, 728-741 (2010).
979 38. A. Fokine *et al.*, Structure and Function of Hoc - A Novel Environment Sensing Device Encoded by
980 T4 and Other Bacteriophages. *Viruses* **15**, 1517 (2023).
981 39. Q. Fang *et al.*, Structures of a large prolate virus capsid in unexpanded and expanded states
982 generate insights into the icosahedral virus assembly. *Proc. Natl. Acad. Sci. U.S.A.* **119**,
983 e2203272119 (2022).
984 40. J. L. Liu, A. B. Dixit, K. L. Robertson, E. Qiao, L. W. Black, Viral nanoparticle-encapsidated enzyme
985 and restructured DNA for cell delivery and gene expression. *Proc. Natl. Acad. Sci. U.S.A.* **111**,
986 13319-13324 (2014).
987 41. J. M. Mullaney, L. W. Black, Capsid targeting sequence targets foreign proteins into bacteriophage
988 T4 and permits proteolytic processing. *J. Mol. Biol.* **261**, 372-385 (1996).
989 42. J. M. Mullaney, L. W. Black, Bacteriophage T4 capsid packaging and unpackaging of DNA and
990 proteins. *Methods Mol. Biol.* **1108**, 69-85 (2014).
991 43. P. Tao, X. Wu, W. C. Tang, J. Zhu, V. Rao, Engineering of Bacteriophage T4 Genome Using CRISPR-
992 Cas9. *ACS Synth. Biol.* **6**, 1952-1961 (2017).

993 44. Y. Liu *et al.*, Covalent modifications of bacteriophage genome confer a degree of resistance to
994 bacterial CRISPR systems. *J. Virol* **94**, e01630-20 (2020).
995 45. J. Zhu *et al.*, A Bacteriophage-Based, Highly Efficacious, Needle- and Adjuvant-Free, Mucosal
996 COVID-19 Vaccine. *mBio* **13**, e01822-01822 (2022).
997 46. M. Rao *et al.*, Highly effective generic adjuvant systems for orphan or poverty-related vaccines.
998 *Vaccine* **29**, 873-877 (2011).
999 47. Q. Li, S. B. Shivachandra, Z. Zhang, V. B. Rao, Assembly of the small outer capsid protein, Soc, on
1000 bacteriophage T4: a novel system for high density display of multiple large anthrax toxins and
1001 foreign proteins on phage capsid. *J. Mol. Biol.* **370**, 1006-1019 (2007).
1002 48. P. Tao *et al.*, Mutated and bacteriophage T4 nanoparticle arrayed F1-V immunogens from Yersinia
1003 pestis as next generation plague vaccines. *PLoS Pathog.* **9**, e1003495 (2013).
1004 49. J. Zhu *et al.*, A universal bacteriophage T4 nanoparticle platform to design multiplex SARS-CoV-2
1005 vaccine candidates by CRISPR engineering. *Sci. Adv.* **7**, eabh1547 (2021).
1006 50. M. Li *et al.*, T4 bacteriophage nanoparticles engineered through CRISPR provide a versatile
1007 platform for rapid development of flu mucosal vaccines. *Antiviral Res.* **217**, 105688 (2023).
1008 51. A. H. Keeble *et al.*, Approaching infinite affinity through engineering of peptide-protein interaction.
1009 *Proc. Natl. Acad. Sci. U.S.A.* **116**, 26523-26533 (2019).
1010 52. A. J. Greaney *et al.*, Complete Mapping of Mutations to the SARS-CoV-2 Spike Receptor-Binding
1011 Domain that Escape Antibody Recognition. *Cell Host Microbe* **29**, 44-57.e49 (2021).
1012 53. Y.-J. P. Alexandra C. Walls, M. Alejandra Tortorici, Abigail Wall, Andrew T. McGuire and David
1013 Veesler, Structure, function and antigenicity of the SARS-CoV-2 spike glycoprotein. *Cell* **181**, 281-
1014 292.e6 (2020).
1015 54. A. Grifoni *et al.*, Targets of T Cell Responses to SARS-CoV-2 Coronavirus in Humans with COVID-19
1016 Disease and Unexposed Individuals. *Cell* **181**, 1489-1501.e1415 (2020).
1017 55. N. Le Bert *et al.*, SARS-CoV-2-specific T cell immunity in cases of COVID-19 and SARS, and
1018 uninfected controls. *Nature* **584**, 457-462 (2020).
1019 56. R. L. Hajnik *et al.*, Broad protection and respiratory immunity of dual mRNA vaccination against
1020 SARS-CoV-2 variants. *NPJ Vaccines* **9**, 160 (2024).
1021 57. A. Impagliazzo *et al.*, A stable trimeric influenza hemagglutinin stem as a broadly protective
1022 immunogen. *Science* **349**, 1301-1306 (2015).
1023 58. H. M. Yassine *et al.*, Hemagglutinin-stem nanoparticles generate heterosubtypic influenza
1024 protection. *Nat. Med.* **21**, 1065-1070 (2015).
1025 59. W. Fiers *et al.*, M2e-based universal influenza A vaccine. *Vaccine* **27**, 6280-6283 (2009).
1026 60. L. A. Brito, M. Singh, Acceptable levels of endotoxin in vaccine formulations during preclinical
1027 research. *J. Pharm. Sci.* **100**, 34-37 (2011).
1028 61. T. Mao *et al.*, Unadjuvanted intranasal spike vaccine elicits protective mucosal immunity against
1029 sarbecoviruses. *Science* **378**, eabo2523 (2022).
1030 62. B. Spellberg, J. E. Edwards, Jr., Type 1/Type 2 Immunity in Infectious Diseases. *Clin. Infect. Dis.* **32**,
1031 76-102 (2001).
1032 63. E. Aleebrahim-Dehkordi *et al.*, T helper type (Th1/Th2) responses to SARS-CoV-2 and influenza A
1033 (H1N1) virus: From cytokines produced to immune responses. *Transpl. Immunol.* **70**, 101495
1034 (2022).
1035 64. D. Sterlin *et al.*, IgA dominates the early neutralizing antibody response to SARS-CoV-2. *Sci. Transl.*
1036 *Med.* **13**, (2021).
1037 65. P. N. Boyaka, Inducing Mucosal IgA: A Challenge for Vaccine Adjuvants and Delivery Systems. *J.*
1038 *Immunol.* **199**, 9-16 (2017).
1039 66. K. B. Renegar, P. A. Small, Jr., L. G. Boykins, P. F. Wright, Role of IgA versus IgG in the Control of
1040 Influenza Viral Infection in the Murine Respiratory Tract1. *J. Immunol.* **173**, 1978-1986 (2004).

1041 67. L. Sun, Y. Su, A. Jiao, X. Wang, B. Zhang, T cells in health and disease. *Signal Transduct. Target.*
1042 *Ther.* **8**, 235 (2023).
1043 68. Z. Chen, E. John Wherry, T cell responses in patients with COVID-19. *Nat. Rev. Immunol.* **20**, 529-
1044 536 (2020).
1045 69. A. T. Tan *et al.*, Early induction of functional SARS-CoV-2-specific T cells associates with rapid viral
1046 clearance and mild disease in COVID-19 patients. *Cell Rep.* **34**, 108728 (2021).
1047 70. C. Rydyznski Moderbacher *et al.*, Antigen-Specific Adaptive Immunity to SARS-CoV-2 in Acute
1048 COVID-19 and Associations with Age and Disease Severity. *Cell* **183**, 996-1012.e1019 (2020).
1049 71. S. N. Mueller, T. Gebhardt, F. R. Carbone, W. R. Heath, Memory T Cell Subsets, Migration Patterns,
1050 and Tissue Residence. *Annu. Rev. Immunol.* **31**, 137-161 (2013).
1051 72. P. A. Szabo, M. Miron, D. L. Farber, Location, location, location: Tissue resident memory T cells in
1052 mice and humans. *Sci. Immunol.* **4**, eaas9673 (2019).
1053 73. I. Quast, D. Tarlinton, B cell memory: understanding COVID-19. *Immunity* **54**, 205-210 (2021).
1054 74. A. Alu *et al.*, Intranasal COVID-19 vaccines: From bench to bed. *EBioMedicine* **76**, 103841 (2022).
1055 75. J. Zhu *et al.*, CRISPR Engineering of Bacteriophage T4 to Design Vaccines Against SARS-CoV-2 and
1056 Emerging Pathogens. *Methods Mol. Biol.* **2410**, 209-228 (2022).
1057 76. J. Zhu *et al.*, A prokaryotic-eukaryotic hybrid viral vector for delivery of large cargos of genes and
1058 proteins into human cells. *Sci. Adv.* **5**, eaax0064 (2019).
1059 77. A. K. Drelich *et al.*, Characterization of Unique Pathological Features of COVID-Associated
1060 Coagulopathy: Studies with AC70 hACE2 Transgenic Mice Highly Permissive to SARS-CoV-2
1061 Infection. *PLoS Pathog.* **20**, e1011777 (2024).
1062 78. L. Van Hoecke, E. R. Job, X. Saelens, K. Roose, Bronchoalveolar Lavage of Murine Lungs to Analyze
1063 Inflammatory Cell Infiltration. *J. Vis. Exp.* **4**, 55398 (2017).
1064 79. R. R. G. Machado *et al.*, Immunogenicity and efficacy of vaccine boosters against SARS-CoV-2
1065 Omicron subvariant BA.5 in male Syrian hamsters. *Nat. Commun.* **14**, 4260 (2023).
1066 80. B. L. Tiner *et al.*, Immunisation of two rodent species with new live-attenuated mutants of Yersinia
1067 pestis CO92 induces protective long-term humoral- and cell-mediated immunity against
1068 pneumonic plague. *NPJ Vaccines* **1**, 16020 (2016).
1069 81. K. Sun, L. Torres, D. W. Metzger, A detrimental effect of interleukin-10 on protective pulmonary
1070 humoral immunity during primary influenza A virus infection. *J. Virol.* **84**, 5007-5014 (2010).

1071